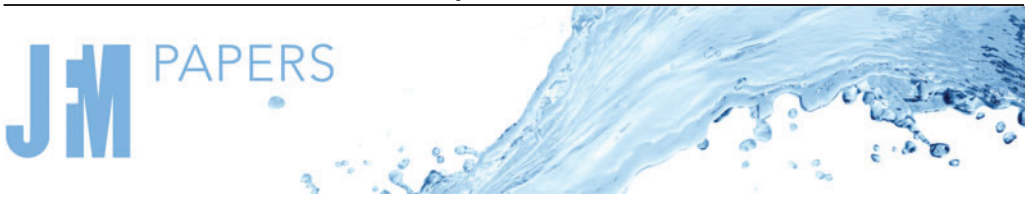
J. Fluid Mech. (2022), *vol*. 949, A18, doi:10.1017/jfm.2022.677



Superhydrophobic surface immobilisation by insoluble surfactant

Michael D. Mayer[1],† **and Darren G. Crowdy**[1]

[1]Department of Mathematics, Imperial College London, 180 Queen's Gate, London SW7 2AZ, UK

(Received 21 March 2022; revised 30 June 2022; accepted 28 July 2022)

The effects of insoluble surfactants, satisfying a Langmuir equation of state, on transverse Stokes flow over a superhydrophobic surface of unidirectional grooves with flat menisci are examined. The phenomenon of surface immobilisation, whereby surfactants cause part or all of the Cassie-state menisci to become effectively no-slip zones thereby degrading the slip properties of the surface, is of primary interest. The study employs a combined analytical and numerical approach allowing an exploration of surfactant effects over the full range of surface Péclet numbers, Marangoni numbers and surfactant loads. For small surface Péclet and Marangoni numbers, perturbation theory is used to gain basic insights into the physical mechanisms at work. That analysis also provides checks on a robust numerical scheme, built around a complex variable formulation of the problem, used to compute solutions across a wide range of non-dimensional parameter values. Two distinct mechanisms are found to be responsible for surface immobilisation. In the first, most commonly seen at higher surface Péclet numbers, a stagnant cap forms because swept surfactant immobilises a section of the meniscus before any portion of the meniscus reaches maximum packing. Such a cap exists even for a linear equation of state and grows in length with increasing Marangoni number. A second immobilisation mechanism is associated with the nonlinear equation of state: an immobilised region forms because the surfactant concentration reaches its maximum value near the downstream edge of the meniscus. Immobilisation of the latter form can occur at much lower surface Péclet numbers, even if the Marangoni number is small, as long as there is sufficient surfactant in the system. The study enhances understanding of how insoluble surfactants can degrade slip over superhydrophobic surfaces.

Key words: drag reduction, coupled diffusion and flow, Marangoni convection

† Email address for correspondence: m.mayer@imperial.ac.uk

© The Author(s), 2022. Published by Cambridge University Press

https://doi.org/10.1017/jfm.2022.677 Published online by Cambridge University Press

1. Introduction

Superhydrophobic surfaces are a class of surfaces which exploit the small-scale effects of surface tension, and the so-called Cassie state, to provide a more slippery environment for flow than would be afforded by a purely no-slip surface (Rothstein 2010; Lee, Choi & Kim 2016). Menisci spanning the gaps between protrusions, asperities or grooves on a surface trap small gas pockets that result in a working fluid sliding over free surfaces rather than being retarded by no-slip contacts. The drag reducing properties of this class of surfaces makes them attractive for a wide range of applications.

These attractive slip properties are easily lost, however. The principal technical challenge is the preservation of the Cassie state: careful pressure control is critical to prevent transition to the alternative Wenzel state where the working fluid invades the gas-filled grooves to cause a fully wetted situation (Rothstein 2010; Lee *et al.* 2016). Recently, other impediments to achieving the desired slip have emerged. Bolognesi, Cottin-Bizonne & Pirat (2014) gave evidence, including effective slip quantification and imaging of the meniscus shape, that superhydrophobic surfaces where the menisci are assumed to be largely free of shear have features suggesting that they are, in fact, closer to being no-slip surfaces. Those authors suggested this slip degradation might be due to the presence of surface contaminants. Shortly after that work, Crowdy (2017*a*) confirmed quantitatively that the data of Bolognesi *et al.* (2014) are indeed more consistent with immobilisation of the menisci. This was done by producing explicit formulae, as a function of protrusion angle, groove width and surface pitch, for the effective slip length assuming the menisci are indeed fully immobilised, and comparing their slip predictions with those from existing formulae in the literature that take the menisci to be shear-free (Crowdy 2017*a*).

The suggestion that surface contaminants are causing loss of slip has recently gained further momentum. Peaudecerf *et al.* (2017) showed that even trace amounts of surfactants can lead to effective immobilisation of a superhydrophobic surface. Consequently, the need to understand when and how a superhydrophobic surface might be immobilised has prompted the formulation of a model for the slip and drag over such surfaces in the presence of surfactants (Landel *et al.* 2020). This quite general model is relevant to soluble surfactants with mass exchange between the surface and the bulk and there is evidence that it offers reliable predictions over a wide range, but not all, of the large parameter space. In particular, the model appears to be least accurate when the parameters are such that immobilisation of parts or all of the menisci has occurred, the case of primary interest in the present paper.

These recent observations on the immobilisation of the menisci in superhydrophobic surfaces are not unrelated of the extensive body of work, spanning many decades, on surfactant effects on the motion of bubbles and drops. For a bubble the phenomenon to be explained is that its rise velocity in a dilute surfactant solution is smaller than that in clean flow and, up to a limit, decreases as the surfactant concentration is increased (Levich 1962). The body of research on this problem has grown incrementally as different effects have been gradually incorporated into both the theoretical and numerical modelling. Excellent reviews of it can be found in Cuenot, Magnaudet & Spennato (1997) and Palaparthi, Papageorgiou & Maldarelli (2006). A notable feature of the retarding mechanism is the formation of what has become known as a ‘stagnant cap’: at large Péclet numbers, and assuming the surfactant to be insoluble, the bulk flow past a rising bubble advects the surfactant to the rear of the bubble so that the surface tension there is smaller than at the front of the bubble. This causes a surface tension gradient on the bubble surface leading to an adverse Marangoni stress which modifies the flow around the bubble, increases the

https://doi.org/10.1017/jfm.2022.677 Published online by Cambridge University Press

drag and retards the bubble. Several theoretical studies of the stagnant cap on a spherical bubble had been carried out using increasing resolution in various poorly convergent series expansions (Savic 1953; Davis & Acrivos 1966) before Sadhal & Johnson (1983) used Abel-like integral transform methods to properly resolve the boundary point singularities at the cap edges. This led to an analytical solution to the problem.

The present investigation, which focuses on transverse flow over a superhydrophobic surface, draws its inspiration from a study by Siegel (1999) on insoluble surfactant effects on the deformation of two-dimensional bubbles of incompressible gas in background extensional flows at zero Reynolds number but at arbitrary capillary number. Siegel devised a numerical method applicable for any surface Péclet number Pe. As Pe gets large, however, it suffers from growing inaccuracies due to emergence of boundary point singularities associated with the formation of stagnant caps. These are the same singularities, albeit in a two-dimensional setting, that plagued the convergence of the series approaches of Savic (1953) and Davis & Acrivos (1966). To address this problem, at infinite surface Péclet number, Siegel (1999) complements his numerical study with the derivation of analytical solutions for the bubble shapes and surfactant distributions in steady equilibrium. These analytical solutions include equilibria exhibiting stagnant caps and involving boundary point singularities where the boundary condition shifts from being one of no-slip to one of no-shear. Siegel uses a complex variable formulation of Stokes flow, and a conformal mapping representation, to formulate his numerical method to track the bubble shapes and the surfactant evolution. To derive the steady analytical solutions with stagnant caps he uses Riemann–Hilbert methods and introduces a set of supplementary functions that capture the boundary point singularities, which happen to be of square-root type, when the stagnant caps form. Crowdy (2013) later showed how modified conformal mapping representations, based on so-called conformal slit mappings (Crowdy 2020*b*), obviate the need for those supplementary singular functions and allow the requisite square-root singularities to be captured in a more intrinsic way by the conformal mapping function itself. This has the significant benefit of removing several numerical difficulties associated with the Riemann–Hilbert approach. The conformal slit mappings of Crowdy (2013) serve the same purpose as the Abel-type transforms used by Sadhal & Johnson (1983) in properly capturing the square-root singularities associated with the change of boundary condition from no-slip to no-shear across the stagnant cap edges. Similar conformal slit mappings have also proven useful in extending the theoretical work of Philip (1972) who analysed mixed boundary value problems relevant to superhydrophobic surfaces. Crowdy (2011) introduced them to extend Philip's solution for flow, both longitudinal and transverse, over a periodic array of no-shear slots to the situation where each period window of the surface contains any geometrical arrangement of no-shear slots, not just one. More recently, Crowdy (2021) used the same conformal slit maps to find slip length formulae for surfaces where the menisci have invaded the grooves and partially fill the cavities.

The study in the present paper also uses a conformal slit mapping description, now as the basis for a robust and easy-to-implement numerical method that will be shown to be effective at capturing surfactant effects on superhydrophobic surfaces over an extensive range of surface Péclet and Marangoni numbers and of interfacial surfactant load. The insoluble surfactant is assumed to satisfy the Langmuir equation of state allowing us to capture important phenomena associated with nonlinear effects in the dependence of surface tension on surfactant concentration. Using this numerical method, here a fairly complete characterisation is given of the flow, the interfacial surfactant concentrations and the effective slip properties as the total surfactant load, the Marangoni numbers and the surface Péclet numbers are varied. The significance of this study is thus threefold.

https://doi.org/10.1017/jfm.2022.677 Published online by Cambridge University Press

First, a novel numerical method is developed using complex analysis techniques that gives high numerical accuracy even for large values of Péclet number. Second, this method is used to generate explicit solutions that span the full parameter space of Péclet and Marangoni numbers for the first time in studies of superhydrophobic surfaces. This provides insight into the transition of interfaces from full-slip interfaces to those that are fully immobilised. Finally, the inclusion of a nonlinear equation of state is shown to introduce a new mechanism for interface immobilisation.

Although there are significant differences in methodology, the physical results of this paper are an extension of results of Baier & Hardt (2021). Those authors investigated the role of insoluble surfactants on immobilising menisci by focusing on the infinite Péclet limit. This limit is known as the stagnant-cap regime because menisci are separated into two regions, a surfactant-laden, immobile region starting on the downstream edge of the interface and a fully mobile region free of surfactant starting on the upstream edge. By using an integral constraint to set the total amount of surfactant, Baier & Hardt (2021) solved for the length of this cap, essentially as a function of Marangoni number. The present paper extends that work by providing results for finite Pećlet numbers and for a nonlinear equation of state.

The structure of the paper is as follows. Having given a formulation of the clean-flow problem in § 3, two useful results on determining the effective slip lengths in general settings using the reciprocal theorem for Stokes flow are described in § 4. The two following sections then give details of a perturbation analysis of the system when the Péclet number Pe is small (in § 5.1) and when the Marangoni number β is small (in § 5.2). This perturbation analysis not only helps elucidate the fundamental physical mechanisms at work, but also provides a non-trivial check on the novel numerical scheme introduced in § 7 based on the complex variable and conformal mapping formulation described in § 6. Section 8 gives a characterisation of the solutions calculated over a wide range of parameter values.

2. Transverse shear flow over superhydrophobic surfaces

Consider the problem of steady transverse simple shear in the semi-infinite region above a periodic row of no-shear slots in an (x, y) plane as shown in figure 1. The slots occupy the interval $[-b, b]$ in a period window $[-a, a]$. In the zero-Reynolds-number regime the fluid velocity $\boldsymbol{u} = (u, v)$ is governed by the Stokes equations

$$\nabla^2 \boldsymbol{u} = \nabla p, \quad \nabla \cdot \boldsymbol{u} = 0, \tag{2.1a,b}$$

where p is the fluid pressure. On the solid ridges the boundary conditions are those of no-slip:

$$u = v = 0, \quad y = 0, b \leq |x| \leq a. \tag{2.2a,b}$$

In a zero-capillary-number limit based on the clean-flow surface tension the meniscus can be taken to be flat with the boundary conditions

$$v = 0, \quad \mu \frac{\partial u}{\partial y} = -\frac{\partial \hat{\sigma}}{\partial x}, \quad y = 0, 0 \leq |x| \leq b, \tag{2.3a,b}$$

where $\hat{\sigma}(x)$ is the local surface tension value. Later we specify how this quantity depends on the local surfactant concentration, denoted by $\hat{\Gamma}(x)$, by specifying an equation of state.

https://doi.org/10.1017/jfm.2022.677 Published online by Cambridge University Press

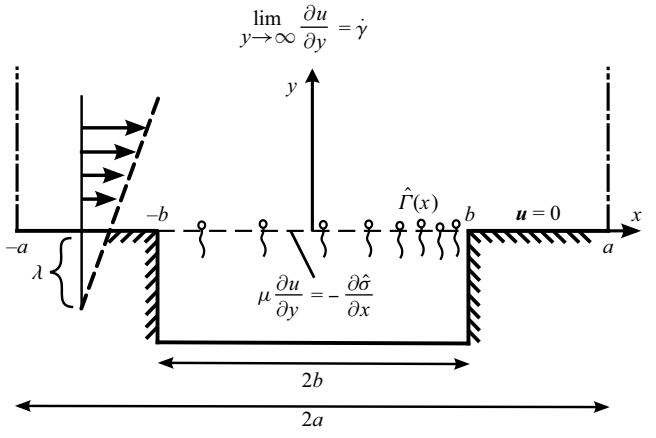


Figure 1. Sketch of the period window of a fluid suspended in the Cassie state over a superhydrophobic surface. The surface is composed of alternating patterns of solid surfaces, or ridges, of length $2a$, between gas-filled cavities of length $2b$. A flat meniscus, with surfactant concentration $\hat{\Gamma}(x)$, spans each cavity. A shear flow is applied over the surface in the direction of the grooves. The surfactant concentration leads to a Marangoni stress on the fluid. Slip is characterised by the effective slip length λ.

As $y \to \infty$, the flow is assumed to have the form

$$(u, v) \to (\dot{\gamma}(y + \lambda), 0), \tag{2.4}$$

where $\dot{\gamma}$ is the imposed far-field shear rate, and λ is the effective slip length which will be used to characterise the degree of slip over the surface. It is usually a positive quantity which can be interpreted as the distance beneath the level $y = 0$ at which the far-field slip velocity (2.4) extrapolates to zero. It measures the slip over the surface caused by the presence of the periodic menisci. For the clean flow problem the slip length is known (Philip 1972; Crowdy 2011) to be given by

$$\frac{a}{\pi} \log \sec\left(\frac{\pi b}{2a}\right). \tag{2.5}$$

This is discussed further in § 3.

The primary interest of this paper is to carefully quantify the effect on the clean-flow slip length (2.5) of contamination of the menisci by insoluble surfactants having a concentration $\hat{\Gamma}(x)$. Let Γ_0 be the maximum packing value of this surfactant concentration. It is natural to introduce the scaled concentration $\Gamma(x)$ where $\Gamma_0\Gamma(x) = \hat{\Gamma}(x)$. If $\Gamma = 0$, the meniscus is clean; if $\Gamma = 1$, it is maximally packed with surfactant. Non-dimensionalising lengths with respect to the half-pitch a and velocities with respect to $U_0 = \dot{\gamma}a$, the non-dimensional steady surfactant evolution equation (Halpern & Frenkel 2003) on the meniscus is

$$Pe\frac{\partial(\Gamma(x)U(x))}{\partial x} = \frac{\partial^2\Gamma(x)}{\partial x^2}, \quad |x| \leq b, \tag{2.6}$$

where $Pe = U_0a/D_s$ is the surface Péclet number, D_s is the surface diffusion parameter and $U(x)$ is the surface slip velocity, i.e. $(u, v) = (U(x), 0)$ on $y = 0$. Henceforth, unless otherwise stated, all variables refer to their non-dimensional counterparts.

It will be assumed that the interfacial surfactant has adsorbed onto the menisci naturally and, consequently, that each meniscus contains the same amount of surfactant; this allows

https://doi.org/10.1017/jfm.2022.677 Published online by Cambridge University Press

us to solve a spatially periodic problem. The total load of surfactant on each meniscus is set by imposing

$$\int_{-b}^{b} \Gamma(x)\,\mathrm{d}x = M, \tag{2.7}$$

where M is some specified quantity. Here it is assumed that $0 \leq M \leq 2b$ with $M = 2b$ corresponding to a meniscus maximally packed with surfactant. At the edges of the meniscus it is natural to take

$$\frac{\partial \Gamma}{\partial x} = 0, \quad x = \pm b, \tag{2.8}$$

corresponding to no flux of surfactant into/out of the solid boundaries; this is reasonable because the pillars are not a source of surfactant. Equation (2.6) can be integrated immediately with respect to x:

$$Pe(\Gamma U) = \frac{\partial \Gamma}{\partial x}, \tag{2.9}$$

where a constant of integration has been set to zero. Then, because $U(\pm b) = 0$, the edge conditions (2.8) will be satisfied.

To close the problem specification it is necessary to invoke an equation of state relating the surface tension $\hat{\sigma}(x)$ to the surfactant concentration $\hat{\Gamma}(x)$. In this paper we assume the nonlinear Langmuir equation of state given, in dimensional form, as

$$\hat{\sigma} = \hat{\sigma}_0 + \hat{\beta}\Gamma_0 \Sigma(\hat{\Gamma}/\Gamma_0), \quad \Sigma(x) = \log(1 - x). \tag{2.10a,b}$$

On introducing the scalings $\hat{\sigma} = \mu U_0 \sigma$ for surface tension and $\hat{\beta} = (\mu U_0/\Gamma_0)\beta$ the equation of state becomes

$$\sigma(x) = \sigma_0 + \beta \Sigma(\Gamma(x)), \quad \Sigma(\Gamma) = \log(1 - \Gamma), \tag{2.11a,b}$$

where we will refer to β as the Marangoni number: it is measure of the strength of the Marangoni stresses relative to the viscous stresses associated with the imposed shear. The linearised version of the equation of state, appropriate when surfactant levels are small, is

$$\sigma(x) \approx \sigma_0 - \beta\Gamma(x). \tag{2.12}$$

This is sometimes referred to as the gaseous equation of state (He, Maldarelli & Dagan 1991). Other equations of state (e.g. the Frumkin equation) can be used but the Langmuir equation (2.11*a*,*b*) is a good representative that affords us certain analytical and formulational advantages while still incorporating important nonlinear effects not captured by the linearised form (2.12).

The problem of characterising surface immobilisation, and the concomitant reduction in slip, for such a nonlinear equation of state is very rich. Note that on substitution of (2.11*a*,*b*) into (2.3*a*,*b*), the local Marangoni stress opposing the imposed shear flow is

$$\frac{\beta}{1 - \Gamma}\frac{\partial \Gamma}{\partial x}. \tag{2.13}$$

If this quantity becomes large it has an adverse effect on the flow and can potentially immobilise the meniscus. The quantity (2.13) can become significant for three different reasons: if the parameter β (the Marangoni number) is itself large, or if the surfactant gradient $\partial\Gamma/\partial x$ is large, or if Γ is close to unity. Which one, or mixture, of these circumstances pertains is a delicate function of the surface Péclet number and total surfactant load M as explored in § 8.

https://doi.org/10.1017/jfm.2022.677 Published online by Cambridge University Press

3. The clean-flow problem

For the clean-flow problem the solution to the mixed boundary problem just described was determined in analytical form by Philip (1972) using Schwarz–Christoffel theory and by Crowdy (2011) using an alternative derivation based on conformal slit mappings. It is the latter formulation that we now describe because the numerical method for the surfactant-contaminated problem described in § 7 is built on it. Crowdy (2011) has shown that the flow in the clean-flow scenario is described by the streamfunction

$$\psi(x, y) = \mathrm{Im}[\bar{z} f_P(z; b) + g_P(z; b)], \quad u = \frac{\partial \psi}{\partial y}, \quad v = -\frac{\partial \psi}{\partial x}, \tag{3.1a–c}$$

where $z = x + \mathrm{i}y$ and

$$g_P(z; b) = -z f_P(z; b), \tag{3.2}$$

and where $f_P(z; b, a)$ is given parametrically, in terms of a conformal mapping variable ζ, by

$$\left.\begin{aligned} z = Z(\zeta) &= -\frac{\mathrm{i}}{\pi} \log\left(-\frac{(\zeta - \alpha)(\zeta - 1/\alpha)}{(\zeta - \bar{\alpha})(\zeta - 1/\bar{\alpha})}\right), \quad \alpha = \mathrm{i}\tan\left(\frac{\pi b}{4}\right), \\ f_P(z; b) = F(\zeta) &= \frac{1}{4\pi} \log\left(-\frac{(\zeta - \alpha)(\zeta - 1/\bar{\alpha})}{(\zeta - \bar{\alpha})(\zeta - 1/\alpha)}\right). \end{aligned}\right\} \tag{3.3}$$

An overbar is used to denote complex conjugation. The two functions of ζ appearing as the arguments of the complex logarithms in (3.3) for $Z(\zeta)$ and $F(\zeta)$ are, respectively, a circular slit mapping and a radial slit mapping (Crowdy 2011, 2020*b*). Figure 2 shows the correspondence between points in the upper-half unit ζ disc and points in the principal period window to which it is enough to restrict consideration. The point $\zeta = \alpha$ maps to $y \to +\infty$. The real diameter $\zeta \in [-1, 1]$ is the preimage of the no-slip walls; the upper unit circle $|\zeta| = 1$, $\mathrm{Im}[\zeta] \geq 0$ is the preimage of the meniscus. The edges of the meniscus at $x = \pm b$ correspond to $\zeta = \mp 1$. As $y \to +\infty$, the flow has the form

$$(u, v) \to (y + \lambda_P(b), 0), \quad \lambda_P(b) = \frac{1}{\pi} \log \sec\left(\frac{\pi b}{2}\right), \tag{3.4}$$

where $\lambda_P(b)$ can be found by examining the parametric formulae (3.3) as $\zeta \to \alpha$ as shown in Crowdy (2011). It follows from (3.3) that

$$Z'(\zeta) = \frac{\mathrm{d}Z}{\mathrm{d}\zeta} = -\frac{\mathrm{i}}{\pi} \frac{(\alpha - \bar{\alpha})(1 - |\alpha|^2)(1 - \zeta^2)}{(\zeta - \alpha)(\zeta - \bar{\alpha})(\alpha\zeta - 1)(\bar{\alpha}\zeta - 1)}, \tag{3.5}$$

which will be useful later. These parametric expressions (3.3) give a convenient representation of the solution. As it happens, after some algebra, ζ can be eliminated to give

$$f_P(z; b) = \frac{\mathrm{i}}{2\pi} \cos^{-1}\left(\frac{\cos\left(\frac{\pi z}{2}\right)}{\cos\left(\frac{\pi b}{2}\right)}\right), \quad U_P(x; b) = -2\mathrm{Re}[f_P(z; b)], \tag{3.6a,b}$$

where $U_P(x; b)$ is the slip velocity on $y = 0$. Relations (3.6*a*,*b*) are the results obtained, using very different methods, by Philip (1972).

https://doi.org/10.1017/jfm.2022.677 Published online by Cambridge University Press

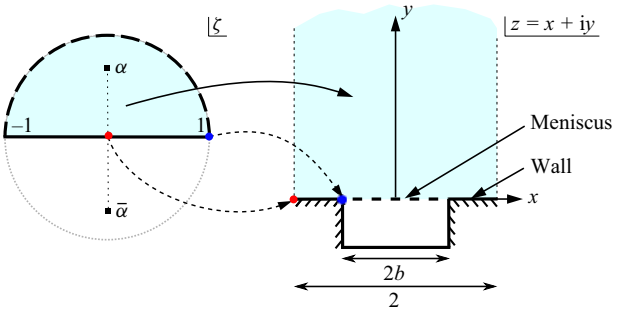


Figure 2. Schematic of the geometrical effect of the conformal mapping $z = Z(\zeta)$ given in (3.3) from the upper-half unit ζ disc to a single period of the fluid region with period $2a$ having set $a = 1$. The numerical method of § 7 will be formulated in the ζ plane. The branch cut (the dotted line) between α and $\bar{\alpha}$ in the upper-half unit disc corresponds to the periodic sides of the fluid region (also dotted lines).

4. Slip length formulae from the reciprocal theorem

Some slip length formulae following from the reciprocal theorem for Stokes flow will be useful in what follows. The reciprocal theorem says that

$$\int_{\partial D} u_i \hat{\sigma}_{ij} n_j \, \mathrm{d}s = \int_{\partial D} \hat{u}_i \sigma_{ij} n_j \, \mathrm{d}s, \tag{4.1}$$

where ∂D is the boundary of the period window D traversed in an anticlockwise sense, $\mathrm{d}s$ is the usual arclength element whereas $\{u_i, \sigma_{ij}\}$ and $\{\hat{u}_i, \hat{\sigma}_{ij}\}$ are two solutions of the Stokes equations in D. The normal vector n_j refers to the outward pointing normal. Let $\{\hat{u}_i, \hat{\sigma}_{ij}\}$ be the velocity and stress tensor for the problem of shear flow over a superhydrophobic surface, with or without surfactants, and let $\hat{\lambda}$ denote the slip length associated with the flow:

$$\hat{\boldsymbol{u}} \to (y + \hat{\lambda}, 0), \quad \text{as } y \to \infty. \tag{4.2}$$

Two useful results follow from (4.1).

The first comes on letting the comparison flow $\{u_i, \sigma_{ij}\}$ in (4.1) be the basic Couette flow $(y, 0)$. Then it follows from (4.1) that

$$\hat{\lambda} = \frac{1}{2} \int_{-b}^{b} \hat{U}(x) \, \mathrm{d}x, \tag{4.3}$$

where $\hat{\boldsymbol{u}} = (\hat{U}(x), 0)$ on $y = 0$.

A second useful result follows on letting the comparison flow $\{u_i, \sigma_{ij}\}$ in (4.1) be the solution (Philip 1972; Crowdy 2011) given in (3.3) or (3.6*a*,*b*) for shear flow over a periodic array of flat no-shear slots without surfactant and with slip length λ_P. In this case,

$$\int_{-b}^{b} u_i \hat{\sigma}_{ij} n_j \Big|_{y=0} \mathrm{d}x - \int_{-1}^{1} u_i \hat{\sigma}_{ij} n_j \Big|_{y\to\infty} \mathrm{d}x = \int_{-b}^{b} \hat{u}_i \sigma_{ij} n_j \Big|_{y=0} \mathrm{d}x - \int_{-1}^{1} \hat{u}_i \sigma_{ij} n_j \Big|_{y\to\infty} \mathrm{d}x, \tag{4.4}$$

where the minus signs have been added because $\mathrm{d}s = -\mathrm{d}x$ along the boundary as $y \to \infty$. Using the shear-free property of $\{u_i, \sigma_{ij}\}$ on the interface it follows that

$$\int_{-b}^{b} u_i \hat{\sigma}_{ij} n_j \Big|_{y=0} \mathrm{d}x = \int_{-1}^{1} u_i \hat{\sigma}_{ij} n_j \Big|_{y\to\infty} \mathrm{d}x - \int_{-1}^{1} \hat{u}_i \sigma_{ij} n_j \Big|_{y\to\infty} \mathrm{d}x = 2(\lambda_P - \hat{\lambda}), \tag{4.5}$$

https://doi.org/10.1017/jfm.2022.677 Published online by Cambridge University Press

or

$$\hat{\lambda} = \lambda_P - \frac{1}{2}\int_{-b}^{b} u_i \hat{\sigma}_{ij} n_j \Big|_{y=0} \,\mathrm{d}x. \tag{4.6}$$

5. Perturbation analysis

Before proceeding, we briefly discuss scalings of the parameters to assess the value of the forthcoming perturbation analyses. Assuming some typical values for the shear rate ($\dot{\gamma} = 0.1\ \mathrm{s}^{-1}$), half-period length ($a = 250 \times 10^{-6}$ m), and the diffusion coefficient [$D = 7 \times 10^{-10}\ \mathrm{m}^2\ \mathrm{s}^{-1}$ that of sodium-decyl sulfate (SDS), an average strength surfactant, see Peaudecerf *et al.* (2017)], it is found that $Pe = \dot{\gamma} a^2/D_s \sim O(10^2)$. This is highly dependent on the choice of length scale. For example, choosing $a = 2 \times 10^{-3}$ m means $Pe \sim O(10^3)$. But smaller length scales and shear rates can lead to Péclet numbers of $O(1)$ or smaller. The choice of $a = 100 \times 10^{-6}$ m with a shear rate of $\dot{\gamma} = 0.01\ \mathrm{s}^{-1}$ means $Pe \sim O(10^0)$, a value small enough such that a small Pe expansion is useful. Some typical values of the Marangoni number ($\beta = \hat{\beta}\Gamma_0/(a\mu\dot{\gamma})$) can also the generated. The dimensional constant $\hat{\beta} = RT$, where R is the universal gas constant and T the liquid temperature in degrees Kelvin, such that $\hat{\beta} \sim O(10^2)$. The maximum packing value is $\Gamma_0 = 3.9 \times 10^{-6}$ mol m^{-2} for SDS. Assuming μ to be the viscosity of water and using the same three parameter sets used to evaluate Pe above, $\beta \sim O(10^6)$ in the case that $Pe \sim O(10^2)$, $\beta \sim O(10^5)$ for $Pe \sim O(10^3)$ and $\beta \sim O(10^7)$ when $Pe \sim O(10^0)$. This scaling indicates that the value of the perturbation analysis for small β may only be in the validating the numerical results; however, the small Pe limit may be a useful result for cases in which the length scales are small.

With these scalings in mind we consider a regular perturbation analysis in two cases: $Pe \ll 1$ and $\beta \ll 1$. This is done to gain insight into the physical mechanisms, particularly the small Pe analysis, and to help evaluate the validity of the later numerical solutions. In each case, considered separately in the next two subsections, having assumed a regular perturbation expansion in each parameter, the validity of that expansion will require restrictions on the other parameters in the problem.

5.1. *Perturbation analysis for small Pe*

First suppose that $Pe \ll 1$ and assume a regular perturbation expansion:

$$\Gamma = \Gamma_0 + Pe\Gamma_1 + \cdots, \quad U = U_0 + PeU_1 + \cdots, \quad \lambda = \lambda_0 + Pe\lambda_1 + \cdots. \tag{5.1a–c}$$

The circumstances under which such a regular expansion is expected to hold will emerge from the analysis. Substitution into (2.9) leads to

$$Pe(\Gamma_0 + Pe\Gamma_1 + \cdots)(U_0 + PeU_1 + \cdots) = \frac{\partial}{\partial x}(\Gamma_0 + Pe\Gamma_1 + \cdots). \tag{5.2}$$

The equation arising at $O(Pe^0)$ is

$$0 = \frac{\partial \Gamma_0}{\partial x}, \tag{5.3}$$

implying that

$$\Gamma_0 = \frac{M}{2b}, \tag{5.4}$$

this constant chosen to satisfy (2.7). Therefore, in the zero surface Péclet limit the surfactant concentration is not affected by the ambient flow and pure diffusion leads to a

https://doi.org/10.1017/jfm.2022.677 Published online by Cambridge University Press

uniform surfactant concentration. This leading-order solution satisfies the edge conditions (2.8). As the associated Marangoni stress is zero the leading-order slip velocity U_0 must be the surface slip velocity in Philip's solution (Philip 1972; Crowdy 2011) with λ_0 the associated slip length:

$$U_0 = U_P(x; b), \quad \lambda_0 = \lambda_P(b). \tag{5.5a,b}$$

At $O(Pe)$ we find from (5.2) that

$$\frac{\partial \Gamma_1}{\partial x} = \Gamma_0 U_0. \tag{5.6}$$

The edge conditions (2.8) require that $\partial \Gamma_1/\partial x = 0$ at $\pm b$ which are satisfied because $U_0 = U_P(x; b)$ which vanishes at the edges $\pm b$ of the no-shear slot. From (5.4), (5.5*a*,*b*) and (5.6) it follows that

$$\Gamma_1(x) = \Gamma_0 \left[\int_{-b}^{x} U_0(x)\, \mathrm{d}x + A \right], \tag{5.7}$$

where A is a constant determined by enforcing (2.7), namely,

$$\int_{-b}^{b} \Gamma_1(x)\, \mathrm{d}x = 0 \text{ or } \int_{-b}^{b} \left[\int_{-b}^{x} U_0(x')\, \mathrm{d}x' \right] \mathrm{d}x + 2bA = 0. \tag{5.8}$$

Using $\hat{\sigma}_{ij}$ to denote the stress tensor associated with the flow the stress condition on the interface can be written

$$\hat{\sigma}_{ij} n_j = \beta \Sigma'(\Gamma) \frac{\partial \Gamma(x)}{\partial x} t_i, \tag{5.9}$$

where t_i denotes components of the unit tangent, and where now n_j refers to the fluid-inward pointing normal. Now provided the quantity

$$\frac{\beta}{1 - \Gamma_0}, \tag{5.10}$$

is of order unity, then, on substitution of (5.1*a–c*) into (5.9), it follows that

$$\hat{\sigma}_{ij} n_j = -\frac{\beta Pe}{1 - \Gamma_0} \frac{\partial \Gamma_1(x)}{\partial x} t_i + O(Pe^2). \tag{5.11}$$

With (5.5*a*,*b*) and (5.6), formula (4.6) gives

$$\lambda = \lambda_P(b) - \frac{Pe \beta \Gamma_0}{2(1 - \Gamma_0)} \int_{-b}^{b} U_P(x; b)^2\, \mathrm{d}x + O(Pe^2). \tag{5.12}$$

This is expected to give a good approximation formula for the effective slip length at small Pe provided the quantity (5.10) is of order unity. It is therefore not expected to be accurate (even if Pe is small) when β is large or for values of M close to its maximum value $2b$ (for which, according to (5.4), Γ_0 is close to unity).

https://doi.org/10.1017/jfm.2022.677 Published online by Cambridge University Press

5.2. *Perturbation analysis for small β*

Suppose instead that $\beta \ll 1$ and assume a different regular perturbation expansion

$$\Gamma = \tilde{\Gamma}_0 + \beta\tilde{\Gamma}_1 + \cdots, \quad U = \tilde{U}_0 + \beta\tilde{U}_1 + \cdots, \quad \lambda = \tilde{\lambda}_0 + \beta\tilde{\lambda}_1 + \cdots. \tag{5.13a–c}$$

On substitution into (2.9), the surfactant evolution equation can be expanded as

$$Pe(\tilde{\Gamma}_0 + \beta\tilde{\Gamma}_1 + \cdots)(\tilde{U}_0 + \beta\tilde{U}_1 + \cdots) = \frac{\partial}{\partial x}(\tilde{\Gamma}_0 + \beta\tilde{\Gamma}_1 + \cdots). \tag{5.14}$$

At $O(\beta^0)$ the equation is

$$Pe(\tilde{\Gamma}_0\tilde{U}_0) = \frac{\partial\tilde{\Gamma}_0}{\partial x}. \tag{5.15}$$

The stress condition becomes

$$\begin{aligned}\left(\frac{\partial\tilde{U}_0}{\partial y} + \beta\frac{\partial\tilde{U}_1}{\partial y}\right) &= \frac{\beta}{1-(\tilde{\Gamma}_0 + \beta\tilde{\Gamma}_1 + \cdots)}\left(\frac{\partial\tilde{\Gamma}_0}{\partial x} + \beta\frac{\partial\tilde{\Gamma}_1}{\partial x} + \cdots\right)\\ &= \beta\left(\frac{1}{1-\tilde{\Gamma}_0} + \frac{\beta\tilde{\Gamma}_1}{(1-\tilde{\Gamma}_0)^2} + \cdots\right)\left(\frac{\partial\tilde{\Gamma}_0}{\partial x} + \beta\frac{\partial\tilde{\Gamma}_1}{\partial x} + \cdots\right).\end{aligned} \tag{5.16}$$

Provided the quantity

$$\frac{1}{1-\tilde{\Gamma}_0}\frac{\partial\tilde{\Gamma}_0}{\partial x}, \tag{5.17}$$

is of order unity, then, at $O(\beta^0)$, (5.16) gives

$$\frac{\partial\tilde{U}_0}{\partial y} = 0, \tag{5.18}$$

which is a zero-shear-stress condition. As the slip velocity must vanish on the no-slip ridges, then, as in § 5.1, we infer once again that the leading-order velocity field is given by Philip's solution so that

$$\tilde{U}_0(x) = U_P(x; b), \quad \tilde{\lambda}_0 = \lambda_P(b). \tag{5.19a,b}$$

The distribution $\tilde{\Gamma}_0(x)$ can now be found by solving (5.15) and using (5.19*a*,*b*):

$$\tilde{\Gamma}_0(x) = \tilde{A}\exp\left(-Pe\int_x^b U_P(x'; b)\mathrm{d}x'\right), \tag{5.20}$$

where the constant $\tilde{A}$ is determined by enforcing (2.7), i.e.

$$\int_{-b}^{b}\tilde{\Gamma}_0(x)\,\mathrm{d}x = M. \tag{5.21}$$

With the same assumption imposed earlier on (5.17), at $O(\beta)$, the stress condition (5.16) gives

$$\frac{\partial\tilde{U}_1}{\partial y} = \frac{1}{1-\tilde{\Gamma}_0}\frac{\partial\tilde{\Gamma}_0}{\partial x}, \tag{5.22}$$

where, given (5.20), the right-hand side is now known implying that the first-order Marangoni stress on the interface is also known. Use of (5.19*a*,*b*), (5.20) and (5.22) in

https://doi.org/10.1017/jfm.2022.677 Published online by Cambridge University Press

(4.6) gives the slip length as

$$\lambda = \lambda_P(b) - \frac{\beta Pe}{2}\int_{-b}^{b} U_P(x;b)^2 \left(\frac{\tilde{A}\exp\left(-Pe\int_x^b U_P(x';b)\,\mathrm{d}x'\right)}{1-\tilde{A}\exp\left(-Pe\int_x^b U_P(x';b)\,\mathrm{d}x'\right)}\right)\mathrm{d}x + O(\beta^2). \tag{5.23}$$

This is expected to be a good approximation for small β provided the quantity (5.17), or equivalently from (5.15), the quantity

$$\frac{Pe\tilde{\Gamma}_0\,\tilde{U}_0}{1-\tilde{\Gamma}_0}, \tag{5.24}$$

is of order unity. Formula (5.23) can therefore be expected to lose accuracy as Pe becomes large, or if $\tilde{\Gamma}_0(x)$ gets close to unity at any point on the meniscus. In such circumstances, the regular perturbation analysis just performed is not expected to be valid. In fact, we can say more as $Pe \to \infty$. In that limit the quantity (5.24) is much larger than unity and we expect the leading-order slip profile U_0 to be quite different from Philip's slip velocity as given in (5.19*a*,*b*): indeed, we expect the slip velocity and slip length at zero Marangoni number to be given by

$$U_P(x;\hat{b}), \quad \text{and} \quad \lambda_P(\hat{b}), \quad 2\hat{b} = 2b - M. \tag{5.25a–c}$$

This is because at infinite surface Péclet number and at zero Marangoni number all surfactant will be advected to the downstream edge of the meniscus with no countervailing Marangoni stress to modify the surfactant concentration, which must satisfy (2.7), from having a jump discontinuity (akin to that of a Heaviside function) as follows:

$$\Gamma(x) = \begin{cases} 0, & -b \le x < b - M, \\ 1, & b - M < x \le b. \end{cases} \tag{5.26}$$

As $0 \le M \le 2b$, the two limiting cases are a clean meniscus as $M \to 0$ and a fully loaded meniscus as $M \to 2b$. These theoretical expectations are borne out by the numerical calculations in § 8.

6. Complex variable formulation

In this section we describe the complex variable approach used by Crowdy (2011) which will provide the basis for a numerical approach to the problem involving insoluble surfactants to be described in § 7; it affords various advantages to be discussed there. Using the non-dimensionalisation introduced earlier, any incompressible Stokes flow in a two-dimensional (x, y) plane is described biharmonic streamfunction $\psi(z, \bar{z})$ given by

$$\psi(z,\bar{z}) = \mathrm{Im}[\bar{z}f(z) + g(z)], \quad (u,v) = \left(\frac{\partial\psi}{\partial y}, -\frac{\partial\psi}{\partial x}\right), \quad u - \mathrm{i}v = 2\mathrm{i}\frac{\partial\psi}{\partial z}, \tag{6.1a–c}$$

where $f(z)$ and $g(z)$ are two functions of $z = x + \mathrm{i}y$. From the Stokes equations it can be shown that the fluid pressure p, the vorticity $\omega = -\nabla^2\psi = -4\partial^2\psi/\partial z\partial\bar{z}$ and the fluid

https://doi.org/10.1017/jfm.2022.677 Published online by Cambridge University Press

rate-of-strain tensor $e_{ij} = (1/2)(\partial u_i/\partial x_j + \partial u_j/\partial x_i)$ are related to $f(z)$ and $g(z)$ through

$$4f'(z) = p - \mathrm{i}\omega, \quad u - \mathrm{i}v = -\overline{f(z)} + \bar{z}f'(z) + g'(z), \quad e_{11} + \mathrm{i}e_{12} = z\overline{f''(z)} + \overline{g''(z)}, \tag{6.2a–c}$$

where primes denote differentiation with respect to the argument of the function. A derivation of these fundamental relations is given in an appendix of Crowdy (2020*a*). The complex form of the fluid stress on the boundary, i.e. $\sigma_{ij} = -pn_i + 2e_{ij}n_j$, is

$$-2\mathrm{i}\frac{\mathrm{d}H}{\mathrm{d}x}, \quad H(z,\bar{z}) \equiv f(z) + z\overline{f'(z)} + \overline{g'(z)}. \tag{6.3a,b}$$

For a far-field simple shear flow with $(u, v) \sim (y + \lambda, 0)$ as $|z| \to \infty$ we need

$$f(z) \sim \frac{\mathrm{i}}{4}z + O(1), \quad g(z) \sim -\frac{\mathrm{i}}{4}z^2 + O(z). \tag{6.4a,b}$$

The choice

$$g(z) = -zf(z), \tag{6.5}$$

is consistent with the far-field shear conditions (6.4*a*,*b*) and ensures that $y = 0$ is a streamline. This means

$$g'(z) = -zf'(z) - f(z). \tag{6.6}$$

It follows from (6.6) that the complex velocity field is

$$u - \mathrm{i}v = -\bar{f} + \bar{z}f'(z) + g'(z) = -\overline{f(z)} + \bar{z}f'(z) - zf'(z) - f(z). \tag{6.7}$$

On $y = 0$, where $\bar{z} = z$, this simplifies to

$$u - \mathrm{i}v = -2\mathrm{Re}[f(z)] := U(x), \tag{6.8}$$

where we introduce $U(x)$ to denote the slip velocity at $y = 0$. The fluid stress on the flat interface must balance the Marangoni stress:

$$\sigma_{ij}n_j = -\frac{\mathrm{d}\sigma(x)}{\mathrm{d}x}t_i. \tag{6.9}$$

From (6.6) it follows that, on $y = 0$,

$$H = f(z) + z\overline{f'(z)} - \overline{zf'(z) + f(z)} = f(z) - \overline{f(z)} = 2\mathrm{i}\,\mathrm{Im}[f(z)], \tag{6.10}$$

and, from (6.3*a*,*b*),

$$-2\mathrm{i}\frac{\mathrm{d}H}{\mathrm{d}x} = 4\frac{\mathrm{d}\,\mathrm{Im}[f(x)]}{\mathrm{d}x} = -\frac{\mathrm{d}\sigma(x)}{\mathrm{d}x} = -\beta\Sigma'(\Gamma)\frac{\mathrm{d}\Gamma}{\mathrm{d}x}. \tag{6.11}$$

Integrating this along the meniscus from the upstream edge at $x = -b$ gives

$$\mathrm{Im}[f(x)] = -\frac{\beta}{4}[\Sigma(\Gamma(x)) - \Sigma(\Gamma(-b))] := \frac{\chi(x)}{2}, \tag{6.12}$$

where we have introduced the new function $\chi(x)$. This integration along the interface is itself significant: it means that, in the numerical method to be described in § 7, the interfacial Marangoni stresses are never actually computed and $f(x)$ depends solely of the absolute difference in dimensionless surface tension between x and the upstream edge $-b$.

https://doi.org/10.1017/jfm.2022.677 Published online by Cambridge University Press

It follows from (6.8) and (6.12) that, on $y = 0$,

$$f(x) = -\frac{U(x)}{2} + \frac{\mathrm{i}\chi(x)}{2}. \tag{6.13}$$

Now introduce the modified analytic function

$$q(z) = -2\mathrm{i}f(z) - \frac{z}{2}, \tag{6.14}$$

which, from (6.4*a*,*b*), is seen to be an analytic function of z in the period window including as $y \to +\infty$. On $y = 0$ it follows from (6.13) that

$$q(x) = \chi(x) - \frac{x}{2} + \mathrm{i}U(x). \tag{6.15}$$

This means that the function $q(z)$ composed with the mapping function, namely,

$$Q(\zeta) \equiv q(Z(\zeta)), \tag{6.16}$$

where $Z(\zeta)$ is given in (3.3), is analytic in the upper-half unit disc including at $\zeta = \alpha$, the preimage of the point at infinity $y \to \infty$.

An important observation from (6.15) is that, on the no-slip wall, corresponding to the real diameter $\bar{\zeta} = \zeta$,

$$0 = U(x) = \mathrm{Im}[q(z)] = \mathrm{Im}[Q(\zeta)]. \tag{6.17}$$

This implies that

$$Q(\zeta) - \overline{Q(\zeta)} = 0, \text{ or } \bar{Q}(\zeta) = Q(\zeta), \tag{6.18}$$

where $\bar{Q}(\zeta) \equiv \overline{Q(\bar{\zeta})}$ is the Schwarz conjugate to $Q(\zeta)$. As $Q(\zeta)$ is analytic in the upper-half unit disc and satisfies (6.18) it follows from the Schwarz reflection principle that $Q(\zeta)$ is analytic everywhere in the unit ζ disc.

It can now be shown (details are given in Appendix A) that $Q(\zeta)$ can be given explicitly on use of the classical Poisson integral formula for the unit disc:

$$Q(\zeta) = \frac{1}{2\pi\mathrm{i}} \oint_{|\zeta'|=1} \frac{\mathrm{d}\zeta'}{\zeta'} \frac{\zeta' + \zeta}{\zeta' - \zeta} \left(\chi(Z(\zeta')) - \frac{Z(\zeta')}{2} \right). \tag{6.19}$$

This formula is important for the numerical method described in § 7: it provides the boundary slip velocity (the imaginary part of $Q(\zeta)$) associated with any given Marangoni stress distribution on the meniscus (which furnishes the real part of $Q(\zeta)$). We note that up to this point in the complex variable formulation no assumptions about Γ have been made. As a consequence (6.19) is valid for any similar problem in which an equation of state for surface tension can be written down.

7. Numerical method based on the conformal mapping formulation

We now describe the numerical scheme. A key step is to pose the Laurent series representation in ζ given by

$$\log\left(\frac{1 - \Gamma(x)}{\Gamma(x)} \right) = b_0 + \sum_{n=1}^{\infty} \left(b_n \zeta^n + \frac{b_n}{\zeta^n} \right), \tag{7.1}$$

where $\{b_n \in \mathbb{R}\}$ is a set of real coefficients to be determined, after suitable truncation, by the numerical algorithm. The representation (7.1) may appear curious at first but several

https://doi.org/10.1017/jfm.2022.677 Published online by Cambridge University Press

features of it should be pointed out because it builds in important requisite properties of the solution. It is worth remarking that several other choices of ansatz were tried before this one, but they all were significantly less robust leading to schemes that failed to converge at much smaller Péclet numbers.

First, as discussed by Crowdy (2011, 2013), use of the conformal mapping variable ζ intrinsically captures the expected square root singularity, as a function of the physical variable z, at the meniscus edges $\pm b$. Written as a function of ζ, however, those singularities do not appear in any explicit way (they have been 'uniformised') and afford a simpler-to-handle Laurent series representation (7.1). This offers both theoretical advantages (Crowdy 2011, 2021) but also significant numerical ones too, as will become evident as the simplicity and effectiveness of the following scheme emerges.

Second, the representation (7.1) automatically builds in the physical requirement

$$0 \leq \Gamma(x) \leq 1. \tag{7.2}$$

If (7.2) fails to be true, it is clear that (7.1) with real coefficients $\{b_n\}$ will not be a consistent representation.

For a given value of b the mapping function (3.3) is known. The first step is to truncate (7.1) at some integer N. A continuation procedure from small values of Pe is then initialised by choosing

$$b_0 = \log\left(\frac{1-\Gamma_0}{\Gamma_0}\right), \quad \Gamma_0 = \frac{M}{2b}, \quad b_n = 0,\ n = 1, \ldots, N, \tag{7.3}$$

where M has been specified. This choice is prompted by the uniform coverage expected at $Pe = 0$ from the perturbation analysis of § 5.1. An analogous continuation procedure can also be carried out as the Marangoni number β is increased from zero using the perturbation analysis of § 5.2 as the initial guess. It follows by straightforward algebraic manipulation of (7.1) that

$$\left.\begin{aligned} \log\Gamma(x) &= -\log\left(1+\exp\left[b_0 + \sum_{n=1}^{N}\left(b_n\zeta^n + \frac{b_n}{\zeta^n}\right)\right]\right), \\ \Gamma(x) &= \left(1+\exp\left[b_0 + \sum_{n=1}^{N}\left(b_n\zeta^n + \frac{b_n}{\zeta^n}\right)\right]\right)^{-1}, \\ \log(1-\Gamma(x)) &= b_0 + \sum_{n=1}^{N}\left(b_n\zeta^n + \frac{b_n}{\zeta^n}\right) - \log\left(1+\exp\left[b_0 + \sum_{n=1}^{N}\left(b_n\zeta^n + \frac{b_n}{\zeta^n}\right)\right]\right), \end{aligned}\right\} \tag{7.4}$$

all of which are needed in what follows. The function $\chi(x)$ can be found from its definition (6.12) and the equation of state (2.11*a*,*b*):

$$\chi(x) = -\frac{\beta}{2}\log\left(\frac{1-\Gamma(x)}{1-\Gamma(-b)}\right), \tag{7.5}$$

which, up to an unimportant constant, is given in terms of the coefficients $\{b_n \in \mathbb{R}\}$ by the final formula in (7.4). As $Z(\zeta)$ is given in (3.3), formula (6.19) can now be used to determine the surface slip $U(x)$, as well as the integral

$$\int_x^b U(x')\,\mathrm{d}x'. \tag{7.6}$$

In practice, use of the Poisson integral formula can be circumvented by use of series expansions and fast Fourier transforms. The reason for computing (7.6) is that, on use

https://doi.org/10.1017/jfm.2022.677 Published online by Cambridge University Press

of an integrating factor in the surfactant evolution equation (2.9), we can write

$$\log \Gamma(x) = \log A_0 - Pe \int_x^b U(x')\,\mathrm{d}x', \tag{7.7}$$

for some constant A_0. Note that, in a step found to be important for robust convergence of the numerical iteration, the integration in (7.7) is taken over an interval that includes the downstream portion of the meniscus that is expected to be contaminated with surfactant in most circumstances.

An important observation is that we now have two expressions for $\log \Gamma(x)$: one is given by the first formula in (7.4), another by (7.7). These are supposed to be consistent when evaluated at the solution. The numerical method is then as follows. Given an initial guess of coefficients $\{b_n | n = 0, 1, \ldots, N\}$, (7.5) is used with (6.19) to determine the surface slip $U(x)$, which is the imaginary part of $Q(\zeta)$, as a Laurent series in ζ. Now (7.6) can be evaluated numerically. This integral is then fed into (7.7) to evaluate $\log \Gamma(x)$. The Laurent series of $\log \Gamma(x)$, valid on $|\zeta| = 1$, as given both by (7.7) and by the first formula in (7.4) are then determined. The required Laurent series coefficients can be readily computed using fast Fourier transforms. A set of N equations to update the initial guess for the truncated set of coefficients $\{b_n | n = 0, 1, \ldots, N\}$ follows by equating powers of ζ^n for $n = 1, \ldots, N$ in these two Laurent series with an additional equation furnished by the mass constraint

$$\int_{-b}^{b} \Gamma(x)\,\mathrm{d}x = M, \tag{7.8}$$

where $\Gamma(x)$ is calculated using the second formula in (7.4). The resulting set of $N + 1$ equations for the $N + 1$ real coefficients $\{b_n | n = 0, 1, \ldots, N\}$ can then be solved. The solutions to follow in § 8 are computed using at most 150 Laurent coefficients, with the majority of the calculations requiring significantly fewer. Usually a quasi-Newton is found to be sufficient to solve for the coefficients but Newton method's is sometimes necessary to ensure convergence when the surfactant load is large.

For small $Pe \ll 1$ a check on the numerical method is to verify that the computed $\Gamma(x)$ agrees, to first order in Pe, with that obtained by the perturbation theory in § 5.1. Similar checks are afforded by the perturbation theory for small β given in § 5.2.

When $Pe \to \infty$ we expect a stagnant cap of length $2b - 2l$ to form adjacent to the downstream edge at $x = b$ where the parameter l can be determined by using Philip's solution (3.6*a*,*b*) and enforcing the condition (7.8). With respect to a shifted frame of reference where the clean portion of the interface now occupies the interval $[-l, l]$ we have

$$\chi(x) = 2\,\mathrm{Im}[f_P(z; l)], \tag{7.9}$$

where f_P is defined in (3.6*a*,*b*) and the contaminated portion of the interface corresponds to the interval $[l, 2b - l]$. For the Langmuir equation of state (2.11*a*,*b*) we have

$$\Gamma(x) = 1 - \mathrm{e}^{-2\chi(x)/\beta}, \tag{7.10}$$

so (7.8), which is a single nonlinear equation for l, is

$$\int_l^{2b-l} (1 - \mathrm{e}^{-4\,\mathrm{Im}[f_P(z;l)]/\beta})\,\mathrm{d}x = M. \tag{7.11}$$

Once l is determined from this condition the associated slip length will be

$$\lambda = \lambda_P(l). \tag{7.12}$$

https://doi.org/10.1017/jfm.2022.677 Published online by Cambridge University Press

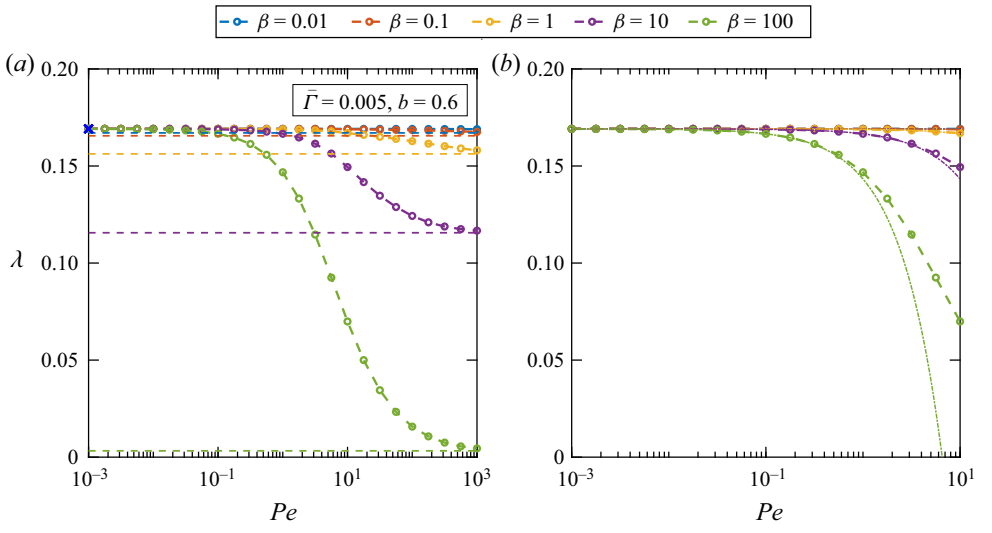


Figure 3. (*a*) Slip length as a function of Pe for different values of β. The horizontal dashed lines show the limit for $Pe \to \infty$ as given by (7.12). (*b*) Refined view of the slip length curves for small Pe. The dotted lines are from the small Pe analysis and are given by (5.12). In both (*a*) and (*b*) $\bar{\Gamma} = 0.005$ and $b = 0.6$.

Details of such a procedure assuming a linear equation of state have been worked out by Baier & Hardt (2021). A completely analogous determination of the edges of two stagnant caps was used by Siegel (1999) for a two-dimensional bubble in an extensional flow, and by Sadhal & Johnson (1983) in a three-dimensional bubble problem.

8. Characterisation of the numerical solutions

The important dimensionless parameters are the surface Péclet number, Pe, the Marangoni number, β, the total amount of surfactant on each meniscus M, and the interface fraction b. A useful parameter in what follows is

$$\bar{\Gamma} = \frac{M}{2b}, \tag{8.1}$$

which represents the average surfactant concentration on the interface.

8.1. *Effect of Pe*

To investigate the effect of Pe on the effective slip lengths, solutions have been calculated for a large range of Pe spanning several decades and for several different values of b, $\bar{\Gamma}$ and β. Figure 3(*a*) shows the slip length over a range of Pe and for five values of β with $\bar{\Gamma} = 0.005$ and $b = 0.6$. As $Pe \to 0$ the slip lengths converge to that of a shear-free meniscus as indicated by the dotted lines in the refined view shown in figure 3(*b*) and corroborating expectations from the perturbation theory of § 5.1. This is because the diffusive flux becomes dominant, yielding a uniform surfactant distribution with no Marangoni stresses. Agreement with the perturbation analysis is good here because, for this choice of parameters, the quantity in (5.10) is of order unity. For this quite small surfactant level $\bar{\Gamma}$ the dashed lines confirm that the solutions converge to give the slip length associated with the $Pe \to \infty$ limit (7.12) discussed at the end of § 7.

Figures 3(*a*) and 3(*b*) also show that, for small β, and for this small value of $\bar{\Gamma} = 0.005$, the slip length is hardly affected by the presence of the surfactant, irrespective of the value

https://doi.org/10.1017/jfm.2022.677 Published online by Cambridge University Press

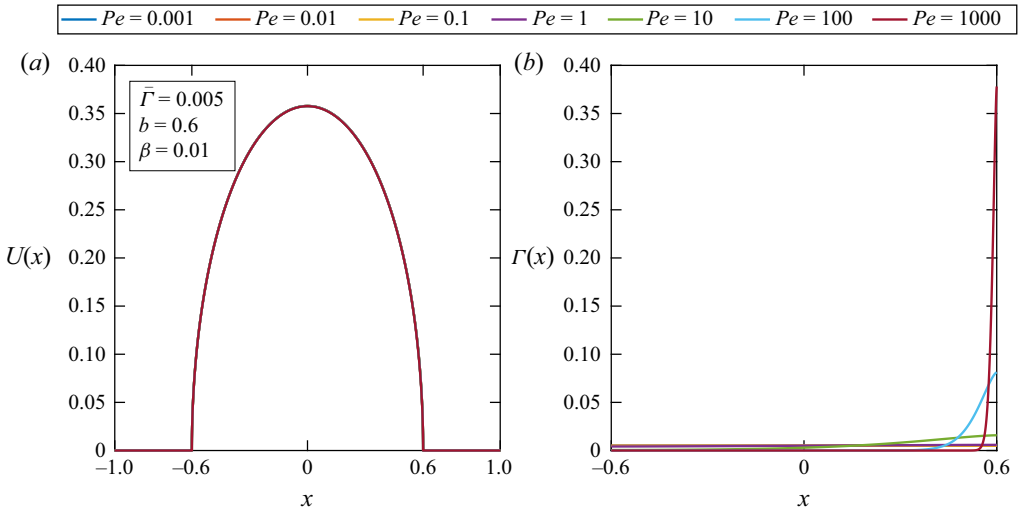


Figure 4. (*a*) Slip velocity profiles and (*b*) surfactant concentrations for different *Pe* with $\bar{\Gamma} = 0.005$, $b = 0.6$ and $\beta = 0.01$.

of *Pe*. As $\bar{\Gamma}$ is small the Langmuir equation of state behaves linearly, i.e. like (2.12), so that when β is small very little shear stress is caused by the surfactant build-up. This means the stagnant cap as $Pe \to \infty$ is expected to be very small. However, we note, as discussed in § 5, that small values of β are not physically representative for these systems so this would be a phenomenon rarely seen in practice. This also explains the limited effect of increasing *Pe* at small values of β. As β increases, however, the shear stresses generated are enough to retard or even nearly immobilise the meniscus at high *Pe*. This causes the dramatic decreases in slip length for larger values of β evident in figure 3(*a*).

Figures 4(*a*) and 4(*b*) show velocity and surfactant concentration profiles at different Péclet numbers when $\beta = 0.01$ for this value of $\bar{\Gamma} = 0.005$. Although the surfactant concentrations in figure 4(*b*) have large gradients at high *Pe*, because β is small these concentrations have very little effect on the slip velocities in 4(*a*). This also explains the limited effect of increasing *Pe* on the slip lengths in figure 3(*a*) for this value of β. For a larger value of β, figures 5(*a*) and 5(*b*) show velocity and concentration profiles for different Péclet numbers when $\beta = 10$. Now β is sufficiently large that the surfactant build up at higher *Pe* retards the flow: there are now noticeably reduced slip velocities at the downstream edge of the meniscus in figure 5(*a*). As $Pe \to \infty$, the section of the domain contaminated with surfactant is immobilised whereas the rest is shear free; this is the expected 'stagnant-cap' regime discussed in § 7. The stagnant cap is even more noticeable in figures 6(*a*) and 6(*b*) which show velocity and concentration profiles for a range of Péclet numbers for the even higher value $\beta = 100$. In this case, β is so large that the meniscus is almost entirely immobilised as *Pe* grows, with only a small section of the meniscus exhibiting any slip by the time $Pe = 1000$. Moreover, in this case, the surfactant concentration tends to a linear profile with slope $(1 - \bar{\Gamma})/\beta$. This happens because the shear stress of a completely immobilised meniscus must equal the far-field shear rate which has been set to unity.

If $\bar{\Gamma}$ is sufficiently large, and/or β is sufficiently small, accumulating surfactant can reach levels close to one and the nonlinearity in the Langmuir equation of state begins to have a more significant effect on the slip properties. As discussed at the end of § 5.2,

https://doi.org/10.1017/jfm.2022.677 Published online by Cambridge University Press

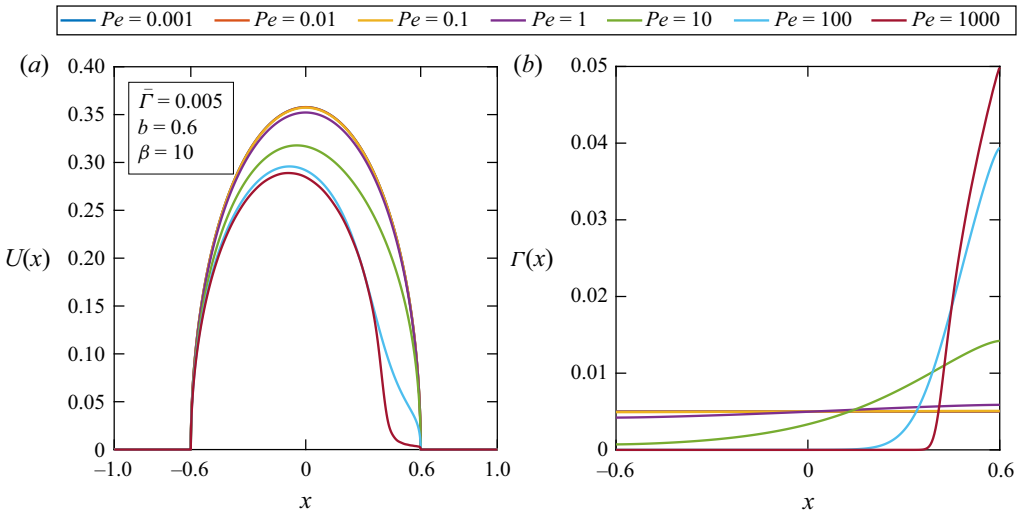


Figure 5. (*a*) Slip velocity profiles and (*b*) surfactant concentrations for different Pe with $\bar{\Gamma} = 0.005$, $b = 0.6$ and $\beta = 10$.

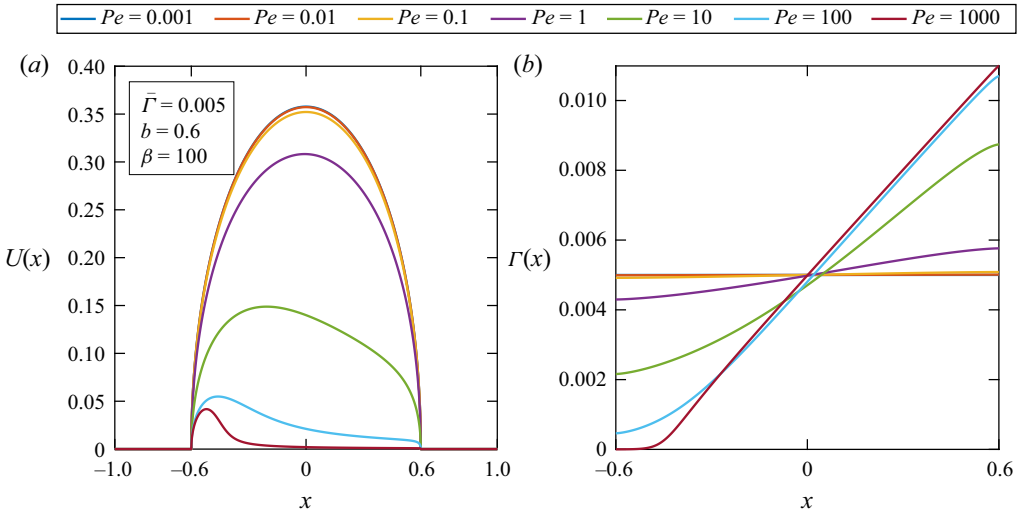


Figure 6. (*a*) Slip velocity profiles and (*b*) surfactant concentrations for different Pe with $\bar{\Gamma} = 0.005$, $b = 0.6$ and $\beta = 100$.

because Γ is capped at unity, the limit as $\beta \to 0$ and $Pe \to \infty$ requires that a stagnant cap of length $M = 2b\bar{\Gamma}$ must form. To explore this further, calculations at increasing values of $\bar{\Gamma}$ are useful.

Figure 7 shows the slip length for a range of Pe, and for different values of β, with $\bar{\Gamma} = 0.05$ and $b = 0.6$. Note on the $\beta = 0.01$ curve of figure 7(*a*) that, at this value of $\bar{\Gamma}$, a noticeable and rapid decrease of slip length is apparent at $Pe \approx 10^{3/2}$, even though β is small. In contrast, at the smaller value $\bar{\Gamma} = 0.005$ shown earlier in figure 3(*a*), the slip length curve shows almost no apparent change as Pe increases. To illuminate the reason for this difference, figures 8(*a*) and 8(*b*) show the slip velocities and surfactant concentrations for $\beta = 0.01$. For $Pe > 100$ the surfactant concentration at the downstream end of the meniscus is seen to be approaching 1, forcing the slip velocity there to decrease.

https://doi.org/10.1017/jfm.2022.677 Published online by Cambridge University Press

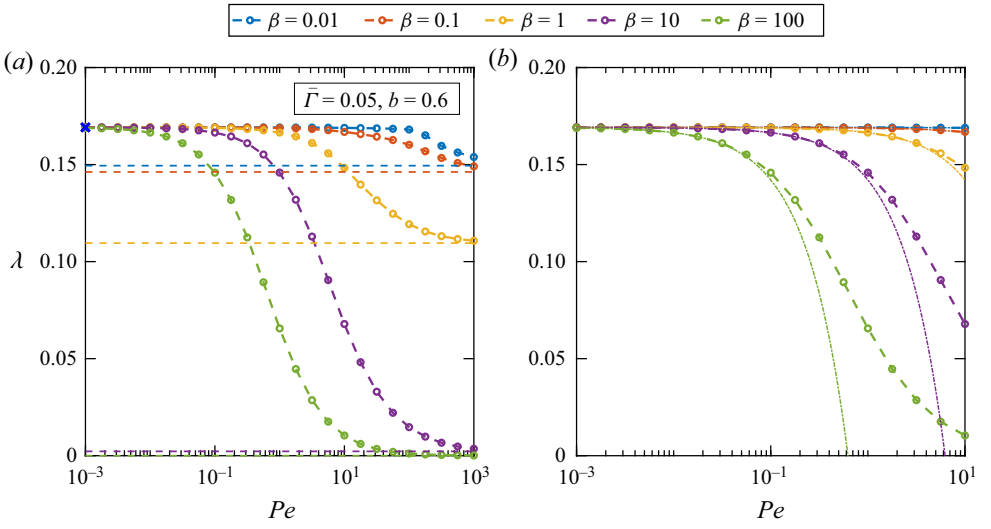


Figure 7. (*a*) Slip length as a function of *Pe* for different values of β with $\bar{\Gamma} = 0.05$ and $b = 0.6$. The horizontal dashed lines show the limit (7.12) for $Pe \to \infty$. (*b*) Refined view of the slip length curves for small *Pe* with dotted lines given by (5.12).

Therefore, as *Pe* increases, the flow transitions rapidly from a pure slip flow (due to the small value of β) to a flow with an immobilised section of the meniscus (due to nonlinear effects associated with Γ reaching its maximally packed value). It is no surprise that the interface portion where $\Gamma \approx 1$ is flat, i.e. $\partial\Gamma/\partial x \approx 0$, since such a balance is clearly necessary in (2.13) to produce a finite Marangoni stress. It is this rapid transition from a slipping flow to one that is partially immobilised that causes the sharp 'elbow', or dipping down, on the $\beta = 0.01$ slip-length curve in figure 7(*a*); note that this elbow is much less pronounced on the other curves shown in figure 7(*a*). At this value of $\bar{\Gamma}$, which can be considered an intermediate value, interaction with the upper limit of Γ is restricted to the smallest value of β. This is because as β grows, the flow becomes retarded enough by the Marangoni stress that the $\Gamma = 1$ ceiling is not reached. This feature is underlined by figure 9 which shows the slip velocities and surfactant concentrations for $\beta = 1$. Although the surfactant concentrations never reach maximum packing at this Marangoni number the flows do nonetheless converge to a stagnant-cap profile at high *Pe*, as expected.

These calculations reveal that, for this nonlinear equation of state, two distinct mechanisms can be responsible for the formation of a stagnant cap. In the first mechanism, seen in figures 5, 6 and 9, a stagnant cap forms because the surfactant immobilises a section of the meniscus before the maximum surfactant concentration is reached. This cap exists even for a linear equation of state and grows in length with increasing β. The second way a cap can form is a result of the nonlinear equation of state, and occurs when Γ nears its ceiling of unity on a portion of the domain. Such a cap is evident in figure 8: it forms because of the large $1/(1-\Gamma)$ factor appearing in the Marangoni stress (2.13). As a general rule of thumb, we have found that such caps tend to occur when β is small, *Pe* is large and $\bar{\Gamma}$ is moderately large. Although this is only a rough characterisation, what is needed is some combination of these three features that lead to the surfactant concentration getting close to one. This second kind of stagnant cap, purely associated with the nonlinear equation of state, means that if there is enough surfactant in a system the meniscus can be severely retarded even for very small values of the Marangoni number β.

https://doi.org/10.1017/jfm.2022.677 Published online by Cambridge University Press

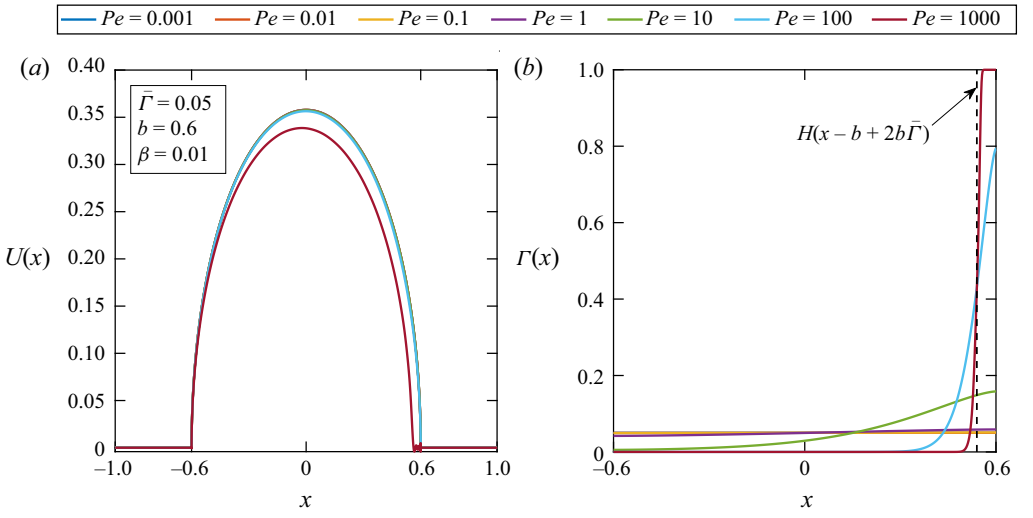


Figure 8. (*a*) Slip velocity profiles and (*b*) surfactant concentrations for different Pe with $\bar{\Gamma} = 0.05$, $b = 0.6$ and $\beta = 0.01$. The vertical dashed line in (*b*) corresponds to the surfactant distribution (5.26) expected in the limit $Pe \to \infty$ and $\beta \to 0$.

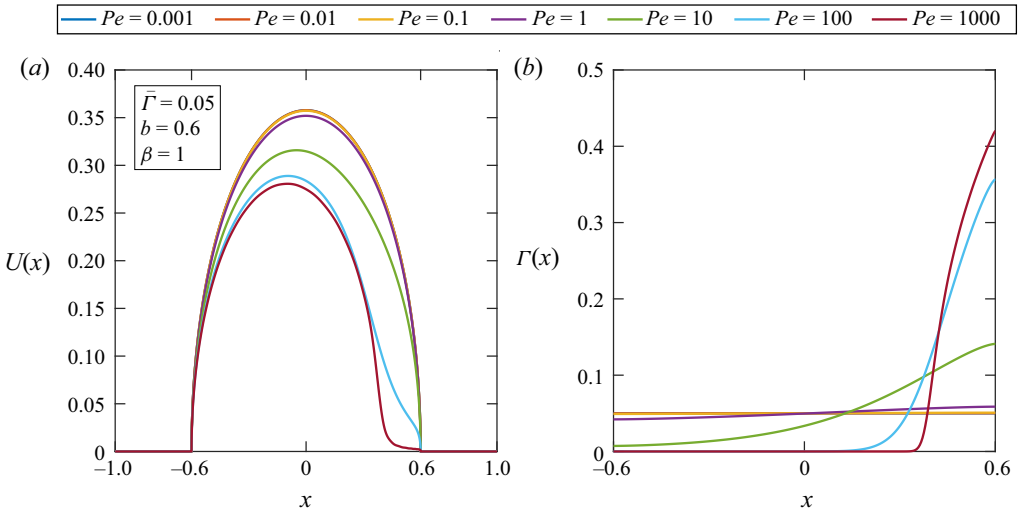


Figure 9. (*a*) Slip velocity profiles and (*b*) surfactant concentrations for different Pe with $\bar{\Gamma} = 0.05$, $b = 0.6$ and $\beta = 1$.

Another important consequence of this type of stagnant cap is that partial immobilisation can occur at lower Pe numbers even if β is small, as long as there is sufficient surfactant in the system.

These effects are further explored in figure 10 which shows slip lengths for a range of Pe and for different values of β with $\bar{\Gamma} = 0.5$ and $b = 0.6$. There is now a significant amount of surfactant on the interface. For $\beta = 0.01$ another elbow can be seen in the graph, akin to that discussed earlier in the $\bar{\Gamma} = 0.05$ case. However, this elbow now occurs at much smaller Pe because even relatively weak advection causes the surfactant concentration to get close to its maximum. The slip lengths in this case are also reduced

https://doi.org/10.1017/jfm.2022.677 Published online by Cambridge University Press

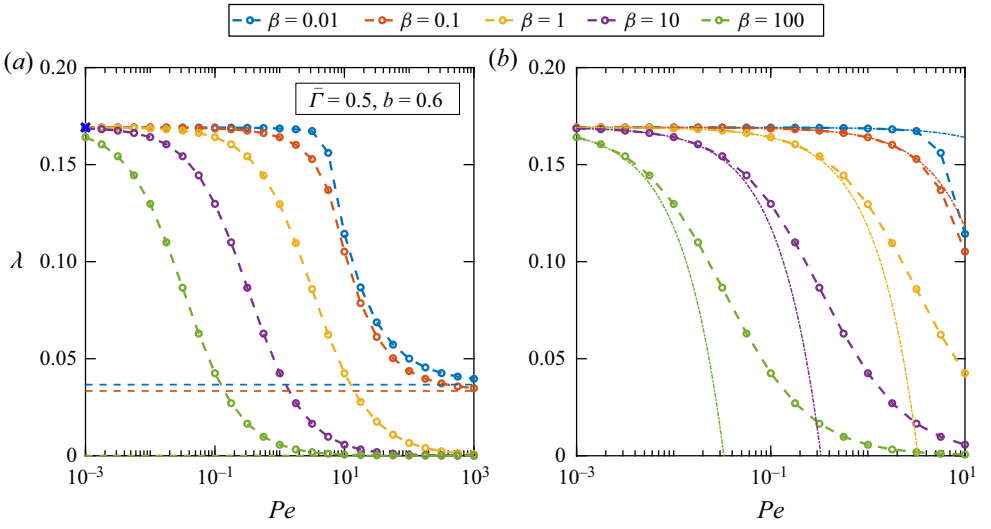


Figure 10. (*a*) Slip length as a function of Pe for different values of β with $\bar{\Gamma} = 0.5$ and $b = 0.6$. The horizontal dashed line corresponds to the $Pe \to \infty$ and $\beta \to 0$ limit (5.25*a–c*). (*b*) Refined view of the slip length curves for small Pe. The dotted lines are results given by (5.12).

significantly compared with the smaller $\bar{\Gamma}$ cases. This is as expected because as $Pe \to \infty$ a stagnant cap should cover half of the domain for small β. To illustrate this, figure 11 shows the slip velocities and surfactant concentrations for $\beta = 0.01$. In figure 11(*b*), the surfactant concentration reaches its ceiling even for Péclet numbers as low as $Pe = 10$, causing significant surface immobilisation as evident in figure 11(*a*). Since $\bar{\Gamma} = 0.5$ and β is small, it is expected that as $Pe \to \infty$ the surfactant accumulates in a stagnant cap occupying half the meniscus. The surfactant concentration can be seen converging to the expected $Pe \to \infty$ and $\beta \to 0$ limit (5.25*a–c*). Figure 11(*a*) also shows an example of some numerical difficulties encountered at large values of Pe. As Pe increases and a stagnant cap forms, a square-root singularity forms at the edge of the stagnant cap. Unlike those at the edges of the meniscus, this emergent square-root singularity is not resolved implicitly by the complex variable formulation, and the number of modes required for an accurate solution increases significantly. Specifically all runs with $Pe = 1000$ were done with $N = 150$ modes, whereas those for most other values required significantly fewer modes, with $N = 10$ being sufficient for low Pe. It is evident from figure 11(*a*) that even $N = 150$ struggles to fully resolve the stagnant-cap singularity, however increasing resolution further was found to reduce the size of the observed numerical oscillations. Adding to the challenge, these simulations at high Pe required a full Newton solve. This culminated in an average of about 10 h per solution on a desktop PC which put a reasonable cap for the solutions at $Pe = 1000$ due to time considerations. Such numerical challenges are, however, to be expected in view of the emergent singularity in the physical system. An interesting avenue of future research is to find a way to incorporate not only the edge-point singularities but also this emergent square-root singularity into the complex variable description to extend the range of the numerical simulation to even higher values of Pe. Nevertheless, that this simple method successfully resolved the system for Péclet numbers as high as the (physically relevant) value of $Pe = 1000$ is noteworthy.

https://doi.org/10.1017/jfm.2022.677 Published online by Cambridge University Press

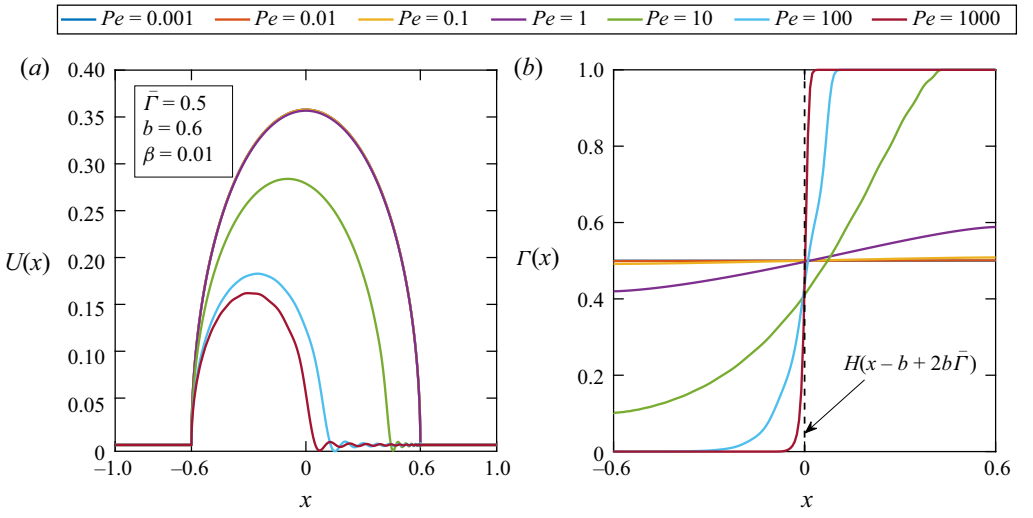


Figure 11. (*a*) Slip velocity profiles and (*b*) surfactant concentrations for different Pe with $\bar{\Gamma} = 0.5$, $b = 0.6$ and $\beta = 0.01$. The vertical dashed line in (*b*) corresponds to the $Pe \to \infty$ and $\beta \to 0$ limit (5.25*a–c*).

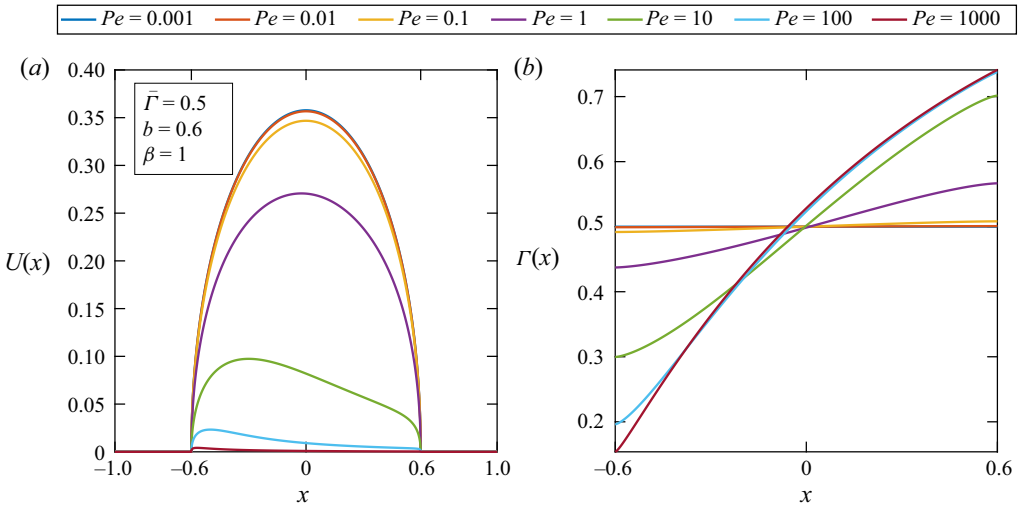


Figure 12. (*a*) Slip velocity profiles and (*b*) surfactant concentrations for different Pe with $\bar{\Gamma} = 0.5$, $b = 0.6$ and $\beta = 1$.

When β is larger, it is less common to reach maximum packing because surfactant gradients tend to be smaller. Figure 12 shows slip velocities and surfactant concentrations for $\beta = 1$. At this relatively large β the balance of surface diffusion and convection is such that the total surfactant concentration does not reach 1 anywhere in the domain. However, the Marangoni stresses are sufficiently large to completely immobilise the meniscus for high Pe values. Finally, figure 13 shows the slip velocities and surfactant concentrations for $\beta = 100$. The slip velocities rapidly shrink to zero as Pe is increased. Moreover, because β is large the surfactant concentration converges to $\Gamma = \bar{\Gamma} + x(1 - \bar{\Gamma})/\beta$. And because $\bar{\Gamma}$ is also large, immobilisation begins to occur when Pe is of order unity. This is because, although small Pe generally yields almost uniform surfactant concentrations, at

https://doi.org/10.1017/jfm.2022.677 Published online by Cambridge University Press

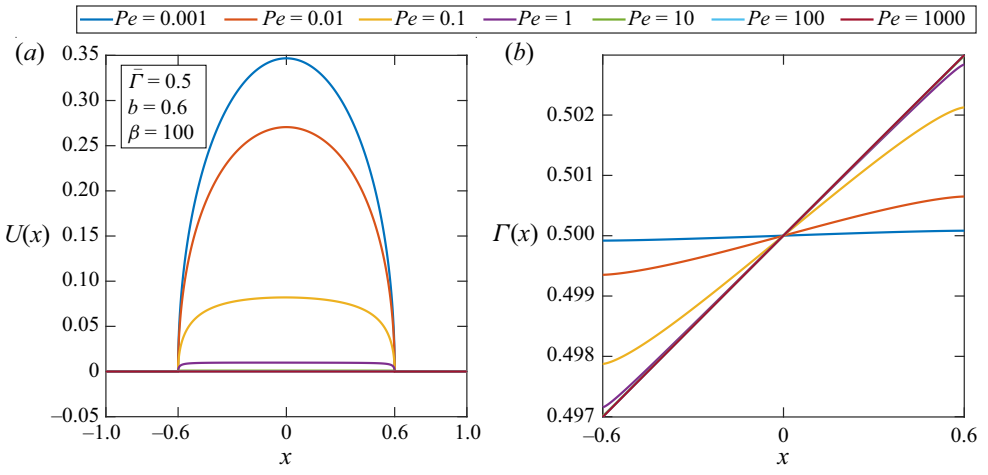


Figure 13. (*a*) Slip velocity profiles and (*b*) surfactant concentrations for different *Pe* with $\bar{\Gamma} = 0.5$, $b = 0.6$ and $\beta = 100$.

high enough values of β and $\bar{\Gamma}$ even small surfactant gradients at low *Pe* cause Marangoni stresses large enough to immobilise the meniscus.

8.2. *Effect of* β

Also of interest is an exploration of how changing β affects the flow. Figure 14 shows the slip length, now as a function of β, for various values of *Pe* with $b = 0.6$ and $\bar{\Gamma} = 0.005$. This figure also shows results from the perturbation analysis for small β given in § 5.2 and from the slip length approximation

$$\lambda \approx \frac{b}{a}\frac{(1-\hat{\Gamma}_0)}{\beta Pe\hat{\Gamma}_0}, \tag{8.2}$$

derived in (B11) from a large-β analysis given in Appendix B.

As $\beta \to 0$, the slip lengths all converge to that of a shear-free meniscus and the perturbation analysis of § 5.2 provides a good approximation as long as *Pe* is order unity or below, which ensures (5.24) is sufficiently small. In fact, for $Pe = 0.01$, there is agreement between the perturbation results and the numerical results up to about $\beta = 10^4$. At larger β the approximation (8.2) matches closely with the numerical results. The slip length vanishes as β increases, regardless of *Pe*, which is expected because eventually β becomes large enough to cause stresses that immobilise the meniscus.

Another interesting effect seen in figure 14 is that because $\bar{\Gamma}$ is small, the effects of β on the flow are weak: indeed very large values of β are needed to fully immobilise the meniscus. When $\bar{\Gamma}$ is larger, smaller values of β are enough to cause immobilisation. To show this, figure 15 shows the slip length, now as a function of β, for various values of *Pe* with $b = 0.6$, but now for the larger value $\bar{\Gamma} = 0.05$. Qualitatively, the results appear similar, with the general shape of the curves looking the same. But the values of β necessary to immobilise the meniscus are reduced by an order of magnitude. This is because the steady state surfactant concentrations for increased amounts of surfactants necessarily have larger gradients, so that a smaller β can create the same stress. One thing that the cases $\bar{\Gamma} = 0.005$ and $\bar{\Gamma} = 0.05$ have in common is that the surfactant level does not reach maximum packing for these values of *Pe*; however, if we increase $\bar{\Gamma}$ even

https://doi.org/10.1017/jfm.2022.677 Published online by Cambridge University Press

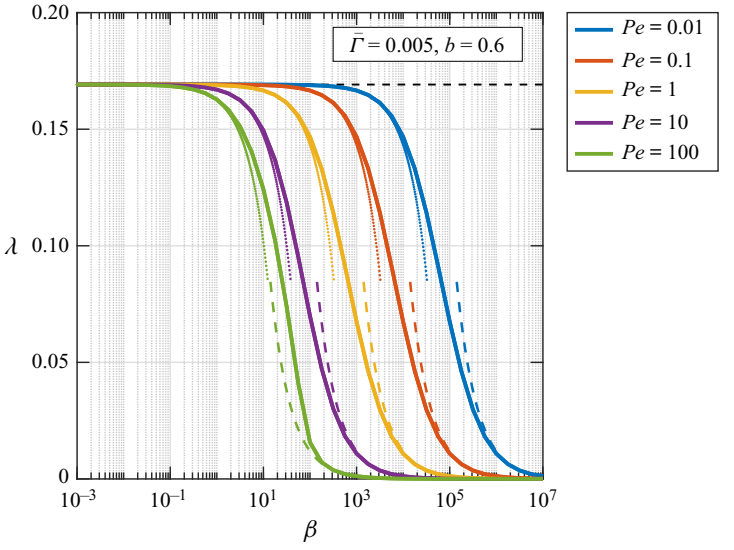


Figure 14. Slip length as a function of β for different values of Pe with $b = 0.6$ and $\bar{\Gamma} = 0.005$. The dotted lines beginning at the top of the figure are from the small β analysis (5.23). The dashed lines towards the bottom of the figure are from (8.2).

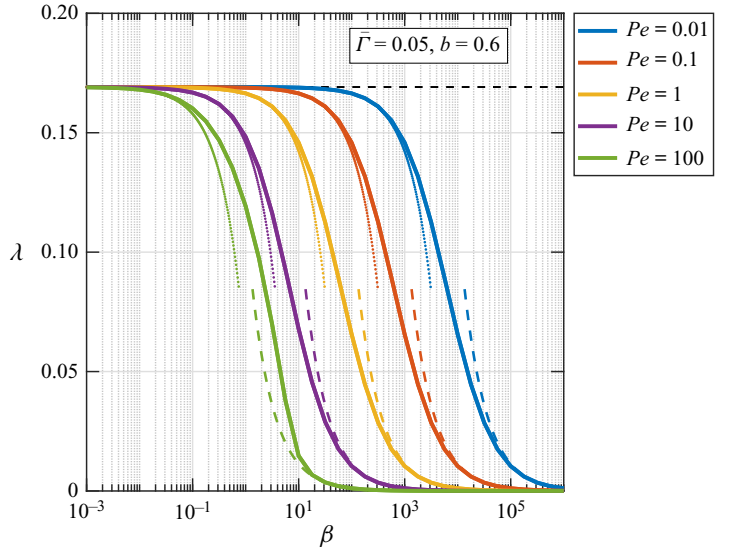


Figure 15. Slip length as a function of β for different values of Pe with $b = 0.6$ and $\bar{\Gamma} = 0.05$. The dotted lines beginning at the top of the figure are from the small β analysis (5.23). The dashed lines towards the bottom of the figure are from (8.2).

further to $\bar{\Gamma} = 0.5$, the nonlinearity of the equation of state has a major effect. Figure 16 shows the slip length, now as a function of β, for various values of Pe with $b = 0.6$ and $\bar{\Gamma} = 0.5$. As Pe increases, the slip lengths no longer converge to those associated by the fully shear-free meniscus. Instead the solutions converge to steady-state flows, dependent on Pe, where part of the meniscus is fully immobilised. This is because of the nonlinearity in the Langmuir equation of state and is consistent with theoretical observations made in

https://doi.org/10.1017/jfm.2022.677 Published online by Cambridge University Press

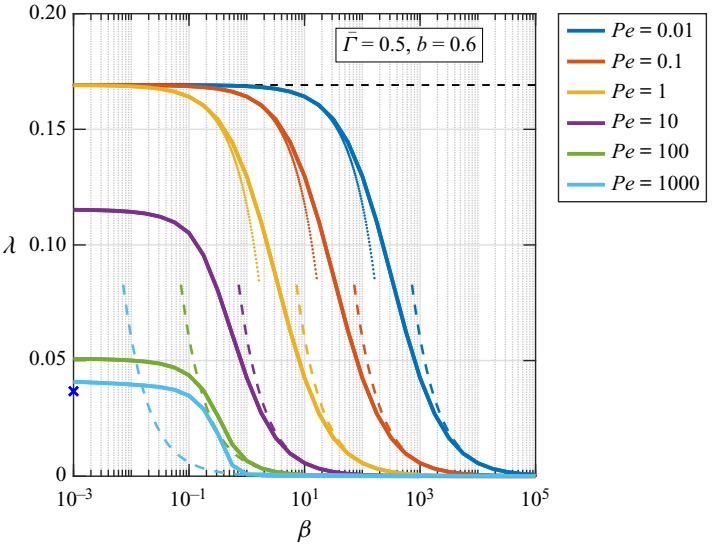


Figure 16. Slip length as a function of β for different values of Pe with $b = 0.6$ and $\bar{\Gamma} = 0.5$. The dotted lines beginning at the top of the figure are from the small β analysis (5.23). The dashed lines towards the bottom of the figure are from (8.2). The blue cross marks the slip length from the $Pe \to \infty$ and $\beta \to 0$ limit (5.25*a–c*).

§ 5.2. For sufficiently small Pe ($Pe = 1$ or lower in figure 16) the numerical results agree well with the perturbation analysis as indicated by the dotted lines; perturbation results for higher Pe are not shown because the agreement is poor. As Pe increases diffusion weakens, whereas as β decreases Marangoni forces weaken. The cumulative effect is that surfactants are free to be swept downstream, accumulating in stagnant caps in near-maximally packed regions where $\Gamma \approx 1$. The blue cross on the axis in figure 16 indicates the slip length value appropriate when $Pe \to \infty$ and $\beta \to 0$ as given by (5.25*a–c*); the slip length at $Pe = 1000$, $\beta = 0.001$ is already close to this value. Figure 17 shows velocity profiles for β values significantly greater than unity; these plots correspond to the flows shown earlier in figure 14. The dashed lines in figure 17 refer to estimates for the velocity from large-β analysis in Appendix B given by

$$U = \frac{(1 - \hat{\Gamma}_0)}{\beta Pe \hat{\Gamma}_0}, \tag{8.3}$$

and derived in (B 10*a*,*b*). Figure 17(*a*), where $Pe = 1$, is a regime where the flow is partially retarded at $\beta = 10^2$ and becomes severely retarded as β grows. The approximation (8.3) does a poor job at $\beta = 10^2$, and leads to severe overestimation of the slip lengths. However, as β increases formula (8.3) becomes increasingly accurate. Figure 17(*b*), for which $Pe = 100$, shows a regime where the flow is nearly fully immobilised; here the approximation (8.3) is in excellent agreement with the velocity profiles. Interestingly, the velocities take on a top-hat shape where velocity assumes a near constant value along most of the interior of the meniscus before rapidly dropping off to zero at the edges.

Concerning the effects of the geometry of the surface, results have been presented here, across the range of surface Péclet, Marangoni numbers and surfactant loads for the particular surface geometry with $b = 0.6$, $a = 1$, but a suite of similar calculations were carried out for $b = 0.8$ and showed qualitatively similar results to those already described.

https://doi.org/10.1017/jfm.2022.677 Published online by Cambridge University Press

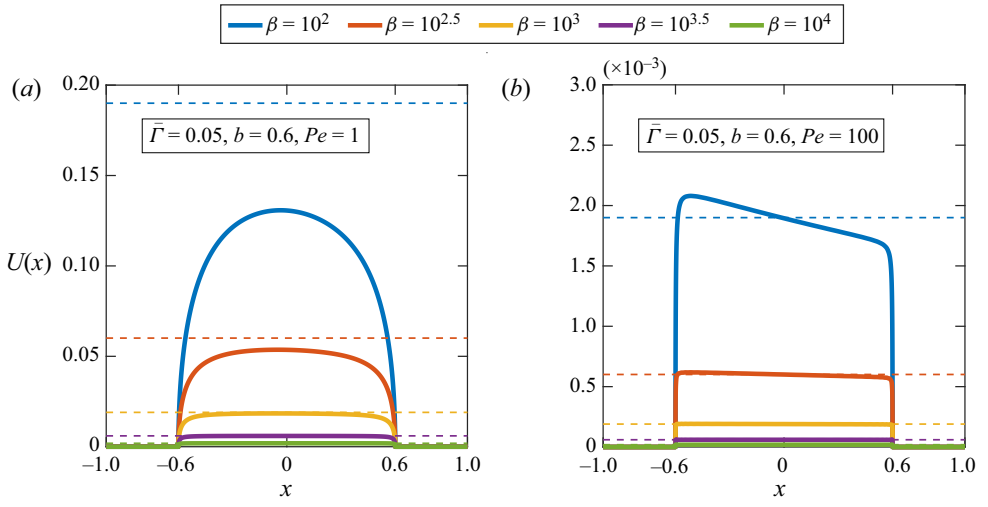


Figure 17. Slip velocity profiles for different (large) β with (*a*) $Pe = 1$ and (*b*) $Pe = 100$ for $\bar{\Gamma} = 0.05$, $b = 0.6$. Dotted lines show the approximation (B10*a*,*b*) of the slip velocity.

9. Discussion

This paper has surveyed the slip properties for transverse flow over superhydrophobic surfaces in the presence of insoluble surfactants, with flat menisci ranging from clean to maximally packed, over the full range of surface Péclet and Marangoni numbers. Focus has been on mechanisms for immobilisation of the interface. Two essentially different mechanisms have been demonstrated: one is characterised by the presence of steep surfactant gradients, the other by the presence of zones of near-maximal packing where, in contrast, surfactant gradients need not be large for significant flow-resisting Marangoni stresses to develop. The mathematical cause of these mechanisms can be seen in the Marangoni stress condition (2.13). The first mechanism has been more widely studied and stems from the term $\beta/(\partial\Gamma/\partial x)$ when the surface tension forces are driven by gradients of surfactant. However, the inclusion here of the effects of the Marangoni number, β, means that steep gradients are not necessary to immobilise menisci. The requirement for immobilisation is a complicated relationship between β and $\partial\Gamma/\partial x$. As a consequence, if β is large, relatively small surfactant gradients are sufficient for complete immobilisation. The second mechanism for immobilisation stems from the term $1/(1-\Gamma)$ in the stress condition. As Γ approaches one, the surface tension forces can grow large, even when gradients of the surfactant are small. The present study is apparently the first to examine this mechanism in the study of superhydrophobic surfaces. When there is a sufficient amount of surfactant, and/or sufficiently low values of β, this means interfaces can be fully or partially immobilised at much lower values of Pe than would be predicted with a linear equation of state.

One limitation in the work here is the use of the Langmuir equation of state. This equation fails to capture the correct surface tension behaviour at large values of Γ. It is well known that surface tension values of interfaces reach a constant value as surfactant concentrations reach the maximum packing density (see e.g. Anna & Mayer 2006). This is because the interface becomes fully packed at $\Gamma = 1$ and surfactant gradients cease to exist. However, Anna & Mayer (2006) showed that this transition to constant surface is very rapid at the maximum packing density; in fact, in their experiments, the Langmuir

https://doi.org/10.1017/jfm.2022.677 Published online by Cambridge University Press

isotherm was still valid for $\Gamma = 0.998$. This suggests many of the results of this paper will remain valid even as Γ approaches one. Moreover, it is worth emphasising that the present formulation can be adapted to any equation of state so that one that correctly captures this behaviour could easily be incorporated.

It is more common to deploy boundary integral methods (Pozrikidis 2010) in the numerical solution to Stokes flow problems, and, while we have eschewed use of these, our own method has an important feature in common with them: it has reduced the two-dimensional Stokes flow problem to a numerical problem posed entirely on the boundary of the domain. Indeed, the method here produces a numerical problem conveniently posed on the unit disc in a parametric ζ plane.

Several extensions of this study can be envisaged. The flow above the surface has been assumed to be a semi-infinite shear flow, whereas it is more usual in practice to find the walls of a finite-width (e.g. microfluidic) channel to be patterned with grooves. Of course, the numerical method based on conformal geometry can be generalised to this case. However, in the absence of surfactants, theoretical evidence exists (Kirk 2018) that the flow close to any such wall in a channel is expected to be well approximated close to the wall (in an inner asymptotic sense) by the flows studied here provided the channel height is larger than the surface pitch. We anticipate that the same will be true if surfactants are added meaning that the flows studied in this paper are also relevant to the channel flow situation.

In this study, the menisci are taken to be flat and flush with the tops of the pillars which make up the no-slip surfaces while the gas pockets are assumed to be inviscid constant pressure regions. Among other effects to be considered are meniscus curvature and subphase fluid effects (Crowdy 2017*b*), as well as the possible depinning of the menisci from the tops of the pillars (Crowdy 2021). How the presence of surfactants affects the slip properties when those additional effects are taken into account is important to quantify. They are perhaps less important, however, than the effects of solubility of the surfactant to the bulk, either to the working fluid or the gas phase, which have also been excluded here. We emphasise, as noted at the end of § 6, that (6.19) is valid contingent only on the existence of an equation of state for surface tension. We therefore expect the complex variable formulation to be of utility too for soluble surfactants. These complicated problems are of particular interest because previous authors (Wang, Papageorgiou & Maldarelli 1999, 2002) have demonstrated that at low Reynolds numbers, the mobility of a surfactant-retarded bubble interface can be increased by raising the bulk concentration of a surfactant which kinetically rapidly exchanges between the surface and the bulk. Quantifying the possible remobilising effect of surfactant solubility is the topic of ongoing work.

Funding. This work is partly funded by EPSRC Grant EP/V062298/1.

Declaration of interests. The authors report no conflict of interest.

Author ORCIDs.
Michael D. Mayer https://orcid.org/0000-0001-7309-5360;
Darren G. Crowdy https://orcid.org/0000-0002-7162-0181.

Appendix A. The solution for $Q(\zeta)$

It was deduced in the main body of the paper that $Q(\zeta)$ is analytic in the unit disc $|\zeta| \leq 1$. It is now useful to ask about the boundary values of $Q(\zeta)$ on C_0. Let C_0^+ denote the semi-circular portion of the unit circle C_0 that lies in the upper-half ζ-plane, and let C_0^-

https://doi.org/10.1017/jfm.2022.677 Published online by Cambridge University Press

denotes the semi-circular portion lying in the lower-half plane. On C_0^+, which corresponds to the meniscus under the mapping $Z(\zeta)$ in (3.3), it follows from (6.15) that

$$\mathrm{Re}[Q(\zeta)] = \chi(Z(\zeta)) - \frac{Z(\zeta)}{2}, \quad \zeta \in C_0^+, \tag{A1}$$

where we recall that $x = Z(\zeta)$ when $\zeta \in C_0^+$. Now suppose that $\zeta \in C_0^-$ so that $\bar{\zeta} \in C_0^+$. Then

$$\mathrm{Re}[Q(\zeta)] = \mathrm{Re}[\overline{Q(\zeta)}] = \mathrm{Re}[\bar{Q}(\bar{\zeta})] = \mathrm{Re}[Q(\bar{\zeta})] = \chi(Z(\bar{\zeta})) - \frac{Z(\bar{\zeta})}{2}, \tag{A2}$$

where, in the penultimate equality, (6.18) has been used and, in the last step, we have used (A1). It can be shown from (3.3) that

$$Z(\bar{\zeta}) = Z(\zeta), \quad \text{for } \zeta \in C_0. \tag{A3}$$

It follows, by combining (A2) and (A3), that

$$\mathrm{Re}[Q(\zeta)] = \chi(Z(\zeta)) - \frac{Z(\zeta)}{2}, \quad \zeta \in C_0^-. \tag{A4}$$

The two conditions (A1) and (A4) together imply

$$\mathrm{Re}[Q(\zeta)] = \chi(Z(\zeta)) - \frac{Z(\zeta)}{2}, \quad \zeta \in C_0. \tag{A5}$$

By these steps, the problem has been reduced to a classical Schwarz problem (Crowdy 2020*b*) for the function $Q(\zeta)$ analytic in the unit disc $|\zeta| < 1$ with known real part on its boundary C_0. The solution is given by the Poisson integral formula

$$Q(\zeta) = \frac{1}{2\pi \mathrm{i}} \oint_{|\zeta'|=1} \frac{\mathrm{d}\zeta'}{\zeta'} \frac{\zeta' + \zeta}{\zeta' - \zeta} \left(\chi(Z(\zeta')) - \frac{Z(\zeta')}{2} \right), \tag{A6}$$

where an additive purely imaginary constant has been set to zero to be consistent with the edge conditions $U(\pm b) = 0$.

Appendix B. Analysis for large Marangoni number β

The numerical calculations reveal that when the Marangoni number β is very large, but not infinite, the velocity on the meniscus takes on a small uniform value, except close to the edges, and the surfactant distribution is close to a constant value with a small slope. The velocity is non-zero because at the triple points the boundary condition $\mathrm{d}\Gamma/\mathrm{d}x = 0$ locally sets the shear stress to zero. This zero-shear-stress condition is incompatible with the expected no-slip condition. This results in two sharp boundary layers near the triple points. Some analysis can help to see why this is the case. Suppose that $\beta \gg 1$ and

https://doi.org/10.1017/jfm.2022.677 Published online by Cambridge University Press

introduce $\epsilon = 1/\beta \ll 1$. Now let

$$\Gamma = \hat{\Gamma}_0 + \epsilon\hat{\Gamma}_1 + \cdots, \quad U = \hat{U}_0 + \epsilon\hat{U}_1 + \cdots, \quad \lambda = \hat{\lambda}_0 + \epsilon\hat{\lambda}_1 + \cdots. \tag{B1a–c}$$

The stress condition can be written as

$$\epsilon\left(\frac{\partial\hat{U}_0}{\partial y} + \epsilon\frac{\partial\hat{U}_1}{\partial y} + \cdots\right) = \frac{1}{1-(\hat{\Gamma}_0 + \epsilon\hat{\Gamma}_1 + \cdots)}\left(\frac{\partial\hat{\Gamma}_0}{\partial x} + \epsilon\frac{\partial\hat{\Gamma}_1}{\partial x} + \cdots\right), \tag{B2}$$

and the surfactant evolution equation becomes

$$\frac{\partial\hat{\Gamma}_0}{\partial x} + \epsilon\frac{\partial\hat{\Gamma}_1}{\partial x} + \cdots = Pe(\hat{\Gamma}_0 + \epsilon\hat{\Gamma}_1 + \cdots)(\hat{U}_0 + \epsilon\hat{U}_1 + \cdots). \tag{B3}$$

At $O(\epsilon^0)$, these two equations give

$$\frac{\partial\hat{\Gamma}_0}{\partial x} = 0, \quad \frac{\partial\hat{\Gamma}_0}{\partial x} = Pe\hat{\Gamma}_0\hat{U}_0. \tag{B4a,b}$$

These are consistent if one takes Couette flow as the leading-order solution for the velocity field:

$$\hat{\boldsymbol{u}}_0(x, y) = (y, 0), \tag{B5}$$

implying $\hat{U}_0(x) = 0$ on $y = 0$. Then

$$\hat{\Gamma}_0 = \frac{M}{2b}, \tag{B6}$$

in order to satisfy both (B3) and (2.7). This choice also satisfies the edge conditions (2.8). At $O(\epsilon)$, (B2) and (B3) give

$$\frac{1}{1-\hat{\Gamma}_0}\frac{\partial\hat{\Gamma}_1}{\partial x} + \frac{\hat{\Gamma}_1}{(1-\hat{\Gamma}_0)^2}\frac{\partial\hat{\Gamma}_0}{\partial x} = \frac{\partial\hat{U}_0}{\partial y}, \quad \frac{\partial\hat{\Gamma}_1}{\partial x} = Pe\hat{U}_1\hat{\Gamma}_0. \tag{B7a,b}$$

Using the leading-order results (B5) and (B6) these become

$$\frac{\partial\hat{\Gamma}_1}{\partial x} = 1 - \hat{\Gamma}_0, \quad \frac{\partial\hat{\Gamma}_1}{\partial x} = Pe\hat{U}_1\hat{\Gamma}_0, \tag{B8a,b}$$

which are consistent provided we take

$$\hat{U}_1 = \frac{(1-\hat{\Gamma}_0)}{Pe\hat{\Gamma}_0}. \tag{B9}$$

Note, however, that the resulting $\partial\hat{\Gamma}_1/\partial x$ fails to satisfy the edge conditions (2.8), but only by an $O(\epsilon)$ amount. We therefore expect the solution over most of the meniscus to be given by

$$U = \frac{(1-\hat{\Gamma}_0)}{\beta Pe\hat{\Gamma}_0}, \quad \Gamma = \frac{M}{2b} + \frac{x}{\beta}, \tag{B10a,b}$$

with small edge corrections near $\pm b$ that will not significantly affect the slip length.

Indeed, using Couette flow as the comparison solution in (4.6), rather than Philip's no-shear/no-slip solution as used in §§ 5.1 and 5.2, an estimate for the slip length is

$$\lambda = \frac{1}{2}\int_{-b}^{b} U(x)\,\mathrm{d}x \approx \frac{b(1-\hat{\Gamma}_0)}{\beta Pe\hat{\Gamma}_0}. \tag{B11}$$

https://doi.org/10.1017/jfm.2022.677 Published online by Cambridge University Press

References

Anna, S.L. & Mayer, H.C. 2006 Microscale tipstreaming in a microfluidic flow focusing device. *Phys. Fluids* **18** (12), 121512.

Baier, T. & Hardt, S. 2021 Influence of insoluble surfactants on shear flow over a surface in Cassie state at large Péclet numbers. *J. Fluid Mech.* **907**, A3.

Bolognesi, G., Cottin-Bizonne, C. & Pirat, C. 2014 Evidence of slippage breakdown for a superhydrophobic microchannel. *Phys. Fluids* **26**, 082004.

Crowdy, D.G. 2011 Frictional slip lengths for unidirectional superhydrophobic grooved surfaces. *Phys. Fluids* **23**, 072001.

Crowdy, D.G. 2013 Surfactant-induced stagnant zones in the Jeong-Moffatt free surface Stokes flow problem. *Phys. Fluids* **25**, 092104.

Crowdy, D.G. 2017*a* Effective slip lengths for immobilized superhydrophobic surfaces. *J. Fluid Mech.* **825**, R2.

Crowdy, D.G. 2017*b* Perturbation analysis of subphase gas and meniscus curvature effects for longitudinal flows over superhydrophobic surfaces. *J. Fluid Mech.* **822**, 307–326.

Crowdy, D.G. 2020*a* Collective viscous propulsion of a two-dimensional flotilla of Marangoni boats. *Phys. Rev. Fluids* **5**, 124004.

Crowdy, D.G. 2020*b* *Solving Problems in Multiply Connected Domains*. Society for Industrial and Applied Mathematics.

Crowdy, D.G. 2021 Slip length formulas for longitudinal shear flow over a superhydrophobic grating with partially filled cavities. *J. Fluid Mech.* **925**, R2.

Cuenot, B., Magnaudet, J. & Spennato, B. 1997 The effects of slightly soluble surfactants on the flow around a spherical bubble. *J. Fluid Mech.* **339**, 25–53.

Davis, R.E. & Acrivos, A. 1966 The influence of surfactants on the creeping motion of bubbles. *Chem. Engng Sci.* **21**, 681–685.

Halpern, D. & Frenkel, A.L. 2003 Destabilization of a creeping flow by interfacial surfactant: linear theory extended to all wavenumbers. *J. Fluid Mech.* **485**, 191–220.

He, Z., Maldarelli, C. & Dagan, Z. 1991 Evidence of slippage breakdown for a superhydrophobic microchannel. *J. Colloid Interface Sci.* **146**, 442–451.

Kirk, T.L. 2018 Asymptotic formulae for flow in superhydrophobic channels with longitudinal ridges and protruding menisci. *J. Fluid Mech.* **839**, R3.

Landel, J.R., Peaudecerf, F.J., Temprano-Coleto, F., Gibou, F. & Goldstein, R.E. 2020 A theory for the slip and drag of superhydrophobic surfaces with surfactant. *J. Fluid Mech.* **883**, A18.

Lee, C., Choi, C.H. & Kim, C.J. 2016 Superhydrophobic drag reduction in laminar flows: a critical review. *Exp. Fluids* **57**, 176.

Levich, V. 1962 *Physicochemical Hydrodynamics*. Prentice Hall.

Palaparthi, R., Papageorgiou, D.T. & Maldarelli, C. 2006 Theory and experiments on the stagnant cap regime in the motion of spherical surfactant-laden bubbles. *J. Fluid Mech.* **559**, 1–44.

Peaudecerf, F.J., Landel, J.R., Goldstein, R.E. & Luzzatto-Fegiz, P. 2017 Traces of surfactants can severely limit the drag reduction of superhydrophobic surfaces. *Proc. Natl Acad. Sci.* **114**, 7254–7259.

Philip, J.R. 1972 Flows satisfying mixed no-slip and no-shear conditions. *J. Appl. Math. Phys.* **23**, 353–372.

Pozrikidis, C. 2010 *Boundary Integral and Singularity Methods for Linearized Viscous Flow*. Cambridge University Press.

Rothstein, J.P. 2010 Slip on superhydrophobic surfaces. *Annu. Rev. Fluid Mech.* **109**, 42–89.

Sadhal, S.S. & Johnson, R.E. 1983 Stokes flow past bubbles and drops partially coated with thin films I: stagnant cap of surfactant film-exact solution. *J. Fluid Mech.* **126**, 237–250.

Savic, P. 1953 Circulation and distortion of liquid drops falling through a viscous medium. *Tech. Rep.* MT-22. Division of Mechanical Engineering, National Research Council Canada.

Siegel, M.I. 1999 Influence of surfactant on rounded and pointed bubbles in two-dimensional Stokes flow. *SIAM J. Appl. Maths* **59**, 1998–2027.

Wang, Y., Papageorgiou, D.T. & Maldarelli, C. 1999 Increased mobility of a surfactant-retarded bubble at high bulk concentrations. *J. Fluid Mech.* **390**, 251–270.

Wang, Y., Papageorgiou, D.T. & Maldarelli, C. 2002 Using surfactants to control the formation and size of wakes behind moving bubbles at order-one Reynolds numbers. *J. Fluid Mech.* **453**, 1–19.

https://doi.org/10.1017/jfm.2022.677 Published online by Cambridge University Press